

**The Impact of Long-Term Glacial Erosion on the Active
Chugach-St. Elias Mountains, southern Alaska**

Jamie Todd Buscher

Thesis submitted to the faculty of the
Virginia Polytechnic Institute and State University
in partial fulfillment of the requirements for the degree of

Master of Science
in
Geosciences

James A. Spotila, Chair
Kenneth A. Eriksson
John A. Hole

October 23, 2003
Blacksburg, Virginia

Keywords: glacial erosion, exhumation, orogeny, AHE dating, Alaska

Copyright 2003, Jamie T. Buscher

The Impact of Long-Term Glacial Erosion on the Active Chugach-St. Elias Mountains, southern Alaska

Jamie Todd Buscher

ABSTRACT

The influence of erosion on uplifting orogens has been demonstrated to be a primary force in landscape development. An understanding of fluvial erosion in mountain belts is fairly well documented, but the impact of glacial erosion is yet to be fully recognized. The uplift of the Chugach-St. Elias Mountains over the last 5-6 Ma under the influence of intense glaciation provides a unique setting to study the impact of glacial erosion on landscape development. The range has been built by rapid convergence (~ 5 cm/yr) of the Yakutat terrane with North America. Climatic forcing of northward-driven storms has created a disproportionate glacier distribution across strike, where extensive piedmont glaciers (low equilibrium line altitudes) cover the windward side of the range and small isolated glaciers (high equilibrium line altitudes) occupy the leeward side. If glacial erosion is greatest at the equilibrium line altitude, then glaciers will act as “buzzsaws” there to limit topographic development. Exhumation would therefore be expected to increase towards the coast. If glacial erosion is not dominant, exhumation would be expected to increase away from the coast towards the core of the range, where fault dip angles are high and deep crustal rocks are exposed.

To determine the impact of long-term glacial erosion on exhumation of the Chugach-St. Elias Mountains, samples were collected along and across the strike of the range and analyzed by the apatite radiogenic helium (AHE) technique. Samples previously dated using the apatite fission track (AFT) method and located adjacent to our field area were also included in the analyses. The low-temperature sensitivity of these thermochronometers allows exhumation rates to be determined for shallow crustal depths. Both glacial and tectonic processes have influenced exhumation of the range. Exhumation rates increase to the south and east towards the collision zone, but coastal rates (0.36-2.5 mm/yr) are significantly higher than inland samples (0.038-0.24 mm/yr). These rates indicate that coastal glaciation plays a dominant role in landscape development and suggest that short-term erosion rates inferred from sediment yields are

exaggerated. Although the exhumation rates are lower than expected, the correlation of exhumation patterns, glacier distribution, and equilibrium line altitude supports the “glacial buzzsaw hypothesis”.

Acknowledgements

I would like to thank everyone who has supported me in my pursuit of studying this remarkable planet. I thank my father, mother, and sister for giving me an appreciation of the outdoors and for always encouraging me to travel to far and away places to look at rocks. I am forever grateful to Mr. Gerald Lewis, Dr. David Douglass, Dr. Janet Gordon, and the rest of the Geology Department at Pasadena City College for sparking my interest in geology. I am indebted to Dr. An Yin (UCLA) and Dr. Eric Cowgill (UC Davis) for giving me the opportunity to experience graduate field work in China while I was an undergraduate at UCLA and for inspiring me to pursue graduate studies in geology. I thank Dr. James Spotila for providing a tremendous amount of guidance and support on the Alaska project and for helping me adjust to graduate school after spending three years in the geotechnical industry. I would also like to thank Dr. Kenneth Eriksson and Dr. John Hole for being on my committee and for providing constructive and thoughtful reviews of my thesis. I have enjoyed my time here at Virginia Tech, and I appreciate everything that the faculty, staff, and graduate students have done to make graduate school a pleasant experience.

Table of Contents

Abstract.....	ii
Acknowledgements.....	iv
Table of Contents.....	v
List of Tables.....	vi
List of Figures.....	vii
Chapters	
1. Introduction.....	1
2. Background.....	7
2.1 Tectonic Background.....	7
2.2 Late Cenozoic Glacial and Sedimentation History.....	17
2.3 Apatite Fission Track (AFT) Data.....	29
3. Methods and Results.....	33
3.1 Apatite Radiogenic Helium (AHE) Technique.....	33
3.2 Results.....	42
4. Interpretations and Discussion.....	52
References Cited.....	68
Vita.....	73

List of Tables

Table 2.1	Accreted terranes, rock types, and corresponding AHE samples from southern Alaska.....	13
Table 3.1	Location and lithology of samples analyzed by AHE.....	38
Table 3.2	AHE data for the Chugach-St. Elias Mountains.....	45-46
Table 4.1	Exhumation rates and T_c depths for AHE samples.....	59

List of Figures

Figure 1.1	Typical landscape features of glaciated orogens.....	6
Figure 2.1	Location of terranes and bounding faults.....	14
Figure 2.2	Cross section of structures and rock types of accreted terranes.....	15
Figure 2.3	Deformed clastic rocks of the Yakutat terrane due to accretion.....	16
Figure 2.4	Impact of glaciers on landscape development.....	21
Figure 2.5	Concentration of large glaciers near high peaks of the Chugach-St. Elias Mountains.....	22
Figure 2.6	Schematic diagram of across-strike glacier distribution.....	23
Figure 2.7	Glacier distribution in the Chugach-St. Elias Mountains.....	24
Figure 2.8	Correlation between ELA and glacial coverage.....	25
Figure 2.9	Correlation between ELA and precipitation.....	26
Figure 2.10	Timing of glacial activity based on data from Yakataga and Poul Creek Formations.....	27
Figure 2.11	Sediment yield vs. basin area for glacial and fluvial settings.....	28
Figure 2.12	AFT sample locations and ages.....	32
Figure 3.1	Temperature and age variations in the HePRZ.....	39
Figure 3.2	AHE and AFT sample locations.....	40
Figure 3.3	Samples collected primarily along ridges.....	41
Figure 3.4	AHE and AFT sample locations and ages.....	47
Figure 3.5	Elevation-distance profiles for AHE and AFT samples.....	48
Figure 3.6	Age vs. distance from coast for AHE and AFT samples.....	49
Figure 3.7	Correlation of age with distance from coast for AHE samples along BB' and CC'.....	50
Figure 3.8	Age-elevation plots for vertical sample suites from northern BB' and CC'.....	51
Figure 4.1	AHE and AFT sample locations and exhumation rates.....	60
Figure 4.2	Contoured exhumation rates for AHE and AFT samples.....	61
Figure 4.3	AHE age-elevation plot for BB' and CC'.....	62
Figure 4.4	AFT age-elevation plot for CC' and DD'.....	63
Figure 4.5	Exhumation rate vs. distance from coast.....	64

Figure 4.6	Comparison of exhumation inferred from AHE data and that expected from tectonics.....	65
Figure 4.7	Correlation of exhumation, ELA, and precipitation.....	66
Figure 4.8	Slope-elevation plot for Chugach-St. Elias Mountains.....	67

CHAPTER 1: INTRODUCTION

In recent years, geoscientists have recognized climate as an important force in landscape development (Molnar and England, 1990; Brozović et al., 1997; Meigs and Sauber, 2000). Orogenic systems at high latitudes, or those that attain sufficiently high altitudes, are dominated by glacial erosion. Mountain landscapes created by glaciers (Figure 1.1), with characteristic jagged alpine peaks, U-shaped valleys, and high sediment yields, are easily distinguished from fluvially-eroded orogens. However, the physical processes of glacial erosion and the effect of glacial erosion on orogenic belts are not yet fully understood.

An emerging paradigm for the role of glaciers in denuding mountains has been called the “glacial buzzsaw hypothesis” (Brozović et al., 1997). This idea holds that negative feedbacks exist between climate, glacial erosion, and uplift, which ultimately control landscape evolution in glaciated mountain belts. One feedback is a cycle where surface uplift increases glacial coverage by climatic forcing, which drives an increase in erosion that limits mountain belt elevation. This partly assumes that glacial erosion is highly effective, and implicitly more effective than fluvial erosion. This is supported by short-term effective erosion rates of 10s of mm/yr in southern Alaska (Hallet et al., 1996). A second negative feedback is where large glaciers lower topography, thus decreasing climatic forcing and limiting the creation of glaciers. The height at which glaciers form in a given climatic regime should thus be significant in mountain belts. The equilibrium line altitude (ELA), where ice accumulation equals ice ablation, represents maximum ice flux, maximum glacial sliding velocity, and possibly the fastest bedrock erosion (Andrews, 1972; Brozović et al., 1997). If the glacial buzzsaw is true, glaciers should limit topography to near ELA (Brozović et al., 1997). Thus, increased glaciation (i.e. lower ELA) should lower topography. In addition, the rates of erosion where glaciers are dominant should scale with rates of rock uplift. Accelerated erosion rates along large established glaciers would create a “glacial aneurysm”, where localized exhumation would limit topographic uplift (Zeitler, 2001).

The topography and glacier distribution of the northwestern Himalaya illustrates this hypothesis (Brozović et al., 1997). Northward-driven monsoonal moisture results in a northward increase in ELA across the range. This correlates with a rise in mean elevation. Hypsometry and slope distribution indicate that a large region of low relief and slope occurs at ELA. This suggests that glaciers limit mountain elevations. Glacial coverage may be more dominant at

controlling hillslope angles than variations in rock type, and therefore can represent the principal control of landscape development at high elevations (or high latitudes) in active mountains.

If true, this hypothesis is important for understanding the evolution of orogenic belts and the interaction of climate and tectonics. Rapid mountain building in the late Cenozoic has been suggested to be primarily a result of climate change (Molnar and England, 1990). Worldwide acceleration in denudation and sediment yields from mountain belts correlate with the timing of global cooling. Increased incision could also drive uplift of mountain peaks (Montgomery, 1994). If alpine glaciers became more expansive in the late Cenozoic and are more efficient at eroding the landscape than fluvial processes, then glaciers might have acted as buzzsaws to rapidly erode orogens. Rapid valley incision could induce an isostatic response that increases mountain belt relief and uplifts mountain peaks (Montgomery, 1994; Small and Anderson, 1995). In contrast, other authors suggest that high sediment yields and increased denudation due to accelerated tectonics could have produced climate change, by increasing CO₂ drawdown (Raymo et al., 1988). The efficiency of glacial erosion is also critical to understanding how erosion and climate affect collision belts. Non-uniform erosion patterns produced by local climatic forcing may lead to partitioning of deformation in orogenic belts (Koons, 1995). Models of subduction and accretionary wedges illustrate how disproportionate erosion across the strike of the range can dictate particle trajectories (Willett and Brandon, 2002). The presence of glaciers may facilitate this, by enabling steady state topography and erosional flux via the buzzsaw. How orogenic belts evolve in glacial climates is thus uncertain.

However, glacial erosion processes over long-term and long-length scales are not well enough understood to evaluate assumptions of the buzzsaw hypothesis. Some studies argue against the buzzsaw hypothesis, suggesting that glaciers play only a minor role in landscape development. For example, a study of glacier profiles suggests that relief production scales with ice thickness, therefore attributing only a small amount of isostatic uplift to glacial erosion (Whipple et al., 1999). In the Sierra Nevada, glacial erosion is also only minimally more effective than fluvial erosion and generates relief only by headward valley erosion (Brocklehurst and Whipple, 2002). Another example of a glaciated mountain belt where the buzzsaw is not well supported is the Southern Alps of New Zealand. Much of the history of this range was dominated by fluvial erosion, with only 20% of total denudation since initial uplift attributed to glacial erosion (Kirkbride and Matthews, 1997). Still, patterns of denudation do not relate to

modern glacier distribution. Landscape development and denudation of the range have been primarily influenced by tectonic uplift associated with the Alpine fault, rather than glaciers (Tippett and Kamp, 1995). Glacial basins are also not greater in denudation or relief in comparison to fluvial basins (Tippett and Kamp, 1995; Kirkbride and Matthews, 1997). Mean topography extends above ELA, suggesting the buzzsaw is not demonstrated (Kirkbride and Matthews, 1997). The relief structure of glaciated basins also implies minimal peak uplift due to glacial incision.

Studies of short-term sediment yields in glaciated orogens, such as Hallet et al. (1996), suggest that glacial erosion is highly effective. Other studies have focused on modern ELA distribution and glacial valley profiles to project the impact of effective short-term glacier erosion on evolving landscapes in the long term (Brozović et al., 1997; Whipple et al., 1999; Meigs and Sauber, 2000; Brocklehurst and Whipple, 2002). However, these studies have not focused on a long-term (10^6 -yr) denudation pattern in a mountain belt dominated by glaciation for most of its development. The quantification of long-term exhumation patterns, particularly with respect to tectonic structures and the distribution of glaciers, would help constrain the influence of glacial erosion on the partitioning of deformation for uplifting orogens and the applicability of the buzzsaw hypothesis. Comparison of the net magnitude of exhumation rates with rates of erosion based on short-term sediment yields would also determine if glacial erosion is temporally non-uniform.

The Chugach-St. Elias Mountains (CSEM) of southern Alaska are ideal for studying the impact of glacial processes on orogenesis. The CSEM have been uplifted since late-Miocene due to local collision and have been glaciated for the past ~ 5 Ma (Plafker, 1987; Lagoe et al., 1993; Plafker et al., 1994b). They are the highest coastal mountain range in the world and the location of previous studies that suggest almost unlimited rates of short-term glacial erosion (Hallet et al., 1996). To determine how glaciation has affected exhumation of this range, rock samples were collected, dated using the apatite radiogenic helium (U-Th/He or AHE) technique, and used to infer long-term exhumation rates. Results show that long-term exhumation rates are much slower than predicted by short-term sediment yields, but also that both tectonic uplift and glacial erosion have influenced landscape development. The buzzsaw hypothesis is thus not supported by extreme rates of glacial erosion but is considered to have played a primary role in coastal areas.

The CSEM are thus a natural place for investigating the interaction of glacial erosion, tectonics, and the buzzsaw hypothesis.

Figure Caption

Figure 1.1 Top picture: Wernicke glacier in the Chugach-St. Elias Mountains. Jagged peaks and high sediment yields typical of glaciated orogens. Glacial erosion occurs upvalley and proglacial stream deposition is dominant downvalley. Bottom picture: Relatively flat glacial valley above steep fluvial valley, illustrating the difference between glacial and fluvial erosion. Looking across Heiden Canyon from Thompson Pass.

Figure 1.1



CHAPTER 2: BACKGROUND

2.1 Tectonic Background

Rapid uplift of the Chugach-St. Elias Mountains (CSEM) since the late Miocene reflects the strong influence of subduction and accretion of the allochthonous Yakutat terrane on the landscape (Plafker, 1987; Lagoe et al., 1993; Plafker et al., 1994b). The inability of the Yakutat terrane to subduct completely beneath the continent while colliding with a constraining, syntaxial bend between the Pacific and North American plates has created peaks over 5000 m high in elevation (Figure 2.1) (Plafker, 1987; Plafker et al., 1994b). Similar accretion of exotic terranes has repeated in southern Alaska since the Mesozoic, resulting in a collage of varying rock types (Table 2.1) and complex structures throughout the CSEM (Figures 2.1 and 2.2) (Plafker, 1987; Plafker et al., 1994b).

The major terranes of the CSEM are shown in Figure 2.1, summarized in Table 2.1 and described at length by Plafker (1987) and Plafker et al. (1994b). The Wrangellia composite terrane (Peninsular, Wrangellia, and Alexander terranes) serves as the backstop for the Southern Margin composite terrane (Chugach, Ghost Rocks, Prince William, and Yakutat terranes). It consists of mid-ocean magmatic-arc rocks that accreted to the North American plate in the mid-Cretaceous and has moved $\sim 30^\circ$ northward since the Eocene. The Chugach terrane consists of three lithologic assemblages that were accreted to the Wrangellia composite terrane in the late-Cretaceous, along a suture represented by the Border Ranges fault. The Ghost Rocks terrane is a 10-km-wide crustal sliver lying predominantly offshore that accreted to the Chugach terrane by 62 Ma, after being displaced $\sim 16^\circ$ northward. Between 62 and 48 Ma, western Alaska rotated counterclockwise and created an oroclinal bend in the plate boundary, forcing the Kula plate to subduct obliquely. Transpression along the continental margin uplifted the Coast Mountains in British Columbia and southern Alaska and triggered significant erosion and sedimentation in deep-sea fan deposits. A magmatic arc formed in the interior of western Alaska, while northward displacement of the Chugach and Ghost Rocks terranes continued along the Denali, Tintina, and Chatham Strait faults. The Prince William terrane consists of the Orca Group and other rocks that collided with the Chugach and Ghost Rocks terranes by 51 Ma, along the modern trace of the Contact fault.

The accretion of the Prince William terrane was followed by several tectonic events that led to ~ 600 km northward displacement of the composite Yakutat terrane into the Gulf of Alaska

(Plafker, 1987; Plafker et al., 1994b). Subduction of the Pacific plate produced andesitic volcanism along the Aleutian arc starting at 50-35 Ma. The dextral Transition fault formed offshore but terminated at 30 Ma, when transform motion moved inland to the dextral Queen Charlotte-Fairweather fault system. This disconnected and translated the Yakutat terrane northwards. This terrane therefore consists partly of oceanic crust and partly of a piece of Chugach terrane that was detached by the Queen Charlotte-Fairweather fault.

Underthrusting, magmatism, and accretion of the northwestward-moving Yakutat terrane into North America created the andesitic Wrangell mountains at ~25 Ma and formed fold and thrust belts, including the Kayak Island Zone, Pamplona Zone, and the Chugach-St. Elias fault (Plafker, 1987; Plafker et al., 1994b). Since ~20 Ma, convergence along the Yakutat-North American plate boundary has produced rapid uplift of the Chugach-St. Elias and Fairweather Ranges. Deformation at the leading edge of the Yakutat terrane has migrated from the northwestern portion of the terrane to the Pamplona Zone in the southeast. Paleomagnetic data indicates that the Yakutat terrane also rotated approximately 20° counterclockwise as it has moved into the syntaxial bend of the Gulf of Alaska, trapped between the Pacific and North American plates.

The Yakutat terrane is bounded on the north by the Chugach-St. Elias fault, on the south by the Transition fault, on the west by the Kayak Island Zone, and on the northeast by the Fairweather fault (Figure 2.1). The terrane is subdivided into three distinct structural and lithologic sections (Plafker, 1987; Plafker et al., 1994b). The northwestern segment consists of a fold-and-thrust belt that extends from the Pamplona Zone to the Aleutian subduction zone. Fold frequency and fault displacements increase where the Yakutat terrane abuts the more cohesive Prince William terrane (Figure 2.2). The central region between the Pamplona Zone and the Dangerous River Zone consists of Paleocene to Oligocene oceanic crust that has been partially fixed to the underthrusting Pacific plate. Cenozoic sediments deposited on the oceanic crust increase in thickness from the middle of the continental slope (6 km) to the inner continental shelf (10 km) and exhibit little to no deformation. East of the Dangerous River Zone, the Yakutat terrane is continental crust, consisting of upper Mesozoic flysch and *mélange* of the Yakutat Group and Tertiary intrusive rocks that have been deformed by right-lateral movement along the Fairweather fault. The Yakutat Group has been metamorphosed to as high as lower greenschist facies and overlain by clastic sediments. The Dangerous River Zone was once the active

Chatham Strait fault, prior to offset by the Queen Charlotte-Fairweather fault system. Structural and lithological features trend parallel to the northwest-striking Fairweather fault and abruptly terminate at the Dangerous River Zone.

The Yakutat terrane is currently moving ~50 mm/yr to the northwest with respect to North America based on plate reconstructions and is only partly coupled to the underlying Pacific plate, which moves oblique to the Fairweather fault at ~55 mm/yr, N17°W (Lahr and Plafker, 1980; DeMets et al., 1990; Plafker et al., 1994b). Global Positioning System data from stations at Yakutat (~44 mm/yr; N37°W) and Cape Yakataga (~38 mm/yr; N32°W) indicate that the Yakutat terrane is moving parallel to the Fairweather fault at lower rates than predicted by plate reconstructions (Sauber et al., 1997; Fletcher and Freymueller, 1999). Geodetic data demonstrate an azimuthal value comparable with Global Positioning System data (N36°W), but a significantly higher plate velocity of 60 mm/yr (Savage and Lisowski, 1988).

Computer models incorporating Very Long Baseline Interferometry help test how active faults within the plate boundary accommodate plate motion (Lundgren et al., 1995; Bird, 1996). Slip rates along the Aleutian megathrust and the Fairweather fault generally decrease towards the compressional syntaxis in the Gulf of Alaska. According to models, the Chugach-St. Elias fault accommodates 20-30 mm/yr of the total Pacific plate motion, leading to crustal thickening within the CSEM. The Transition fault displays little to no movement relative to Pacific-Yakutat plate motion (Lundgren et al., 1995; Bird, 1996). Although models can assign slip rates to the bounding faults, measurements of deformation from field observations and seismic activity are not available, and thus how the northwestward migration of the Pacific plate is accommodated structurally is not well known. Existing constraints are summarized below.

The Kayak Island Zone marks the western boundary of the Yakutat terrane and is believed to represent the northeastern extension of the Aleutian megathrust (Plafker, 1987; Plafker et al., 1994b). It consists of several parallel to subparallel thrust faults that dip to the northwest and are parallel to the Aleutian megathrust. The megathrust ruptured both offshore and onshore with 15 m of offset in 1964, producing a M 9.2 earthquake (Page et al., 1989).

The Fairweather fault defines the dextral Pacific-North American transform plate interface and extends from the eastern end of the Chugach-St. Elias fault to the Queen Charlotte fault in British Columbia (Plafker, 1987; Plafker et al., 1994b). Scarps, displaced drainages, and linear depressions exposed along the fault indicate active dextral movement throughout the

Holocene at rates of 40-50 mm/yr on a 1000-year scale (Plafker et al., 1976). Vertical and dextral offsets (1 m and 3.5 m, respectively) associated with a M 7.9 earthquake in 1958 indicate active transpression and continued uplift of the Fairweather Range.

The Chugach-St. Elias fault represents the northern plate boundary where Eocene clastic rocks of the Yakutat terrane subduct beneath and are accreted to Paleogene metasedimentary rocks of the North American continent (Figure 2.3) (Plafker, 1987; Plafker et al., 1994b; Bruhn et al., in press). The north-dipping fault (30° to 45°) extends along the south side of the St. Elias Mountains from the Kayak Island Zone in the west to the Fairweather fault in the east and is considered active (Plafker, 1987; Estabrook et al., 1992; Plafker et al., 1994b; Bruhn et al., in press). Large magnitude earthquakes in 1899 and 1979 (M 7.9 and 8.0, and M 7.2, respectively) generated by the Chugach-St. Elias fault and other thrusts created measurable uplift in the central portion of the St. Elias Mountains (Estabrook et al., 1992; Bruhn et al., in press). Nearly pure reverse motion is inferred from subsidiary faults and folded rocks of the Yakutat terrane, but limited exposure of the main fault strand makes slip rates difficult to determine (Bruhn et al., in press).

The offshore Transition fault forms the southern boundary of the Yakutat terrane, which extends from the Aleutian megathrust to the Fairweather fault (Plafker, 1987; Plafker et al., 1994b). The role that the Transition fault plays in the overall large-scale tectonics of the region is somewhat elusive, but the fault is thought to be a northward dipping décollement between the Yakutat and Pacific plates (Plafker, 1987; Plafker et al., 1994b; Bruhn et al., in press). Based on the current direction of Pacific plate movement relative to the Transition fault, proximal kinematic data, and earthquake foci, the Transition fault has had minor dextral oblique motion from 5 Ma to the present (Page, 1975; Plafker, 1987; DeMets et al., 1990; Plafker et al., 1994b).

The Border Ranges fault system is a suture where the Chugach terrane was underthrust and accreted to the Wrangellia composite terrane in the late Cretaceous (Plafker, 1987; Plafker et al., 1994b). Strike-slip and normal faults that formed after accretion are found from outside Anchorage to the St. Elias Mountains, indicating the possibility of reactivation.

The Chugach-St. Elias fault and the Transition fault account for up to 30 mm/yr and 10 mm/yr of plate motion, respectively, meaning other secondary faults play an active role in plate accommodation. The Malaspina fault and Pamplona Zone may accommodate significant convergence, based on seismicity and field observations (Estabrook et al., 1992; Bruhn et al., in

press). The Contact fault may also accommodate up to 15 mm/yr, based on Global Positioning System data and seismicity (Estabrook et al., 1992; Sauber et al., 1997). Unfortunately, widespread glaciation and rapid denudation throughout the CSEM has concealed a majority of the active tectonic and geomorphologic features, such that the kinematics of deformation are poorly known.

Collision of the Yakutat terrane into North America and subsequent uplift of the CSEM to elevations over 5000 m in the last 5-6 Ma makes southeastern Alaska an ideal place to study the effects of mountain building on landscape development. High northwestward plate convergence rates coupled with a systematic northward increase in fault dip angles is believed to create a distinct exhumation pattern across strike, where exhumation is greatest in the core of the range. The unique spatial distribution of faults and extensive glacial coverage of the range since uplift began allows the effects of mountain uplift and glacial erosion to be directly compared.

Figure Captions

Table 2.1 Accreted terranes, rock types, and corresponding samples of southern Alaska. Terrane data from Csejtey et al. (1982), Plafker (1987), and Plafker et al. (1994b).

Figure 2.1 Map showing location of terranes and bounding faults. Study area is outlined by black box. Blue dots are AHE sample locations and red squares are AFT sample locations. Circled collision zone represents the approximate area that has been most affected by accretion of Yakutat terrane. Purple area in the northeast portion of the map consists of undifferentiated rocks. Profile AA' is shown in Figure 2.2. Location of terranes from Plafker (1987) and Plafker et al. (1994b). Pacific plate rate from DeMets et al. (1990).

Figure 2.2 Cross section showing structures and rock types of accreted terranes. Figure based on structure and terrane data from Plafker (1987) and Plafker et al. (1994b).

Figure 2.3 Deformed Eocene clastic rocks of the Yakutat terrane seen in the foreground abut Paleogene metasedimentary rocks of the North American continent to the north along the reverse Chugach-St. Elias fault. The recumbent folds illustrate that there is high convergence along the Chugach-St. Elias fault. Bering glacier is located in the middle foreground.

Terrane	Time of Accretion	Lithology	Metamorphic Grade	Assemblages/Units	Dated Samples
Wrangellia Composite (Peninsular, Wrangellia, and Alexander)	Middle Cretaceous	Paleozoic and Mesozoic plutonic, volcanic, metasedimentary, carbonate, and sedimentary rocks	Undifferentiated metamorphic grade	Undifferentiated	01CH4; 02CH1,2,3, 4, 19
Chugach	Late Cretaceous	Late Triassic to Late Cretaceous greenschist, mélange, volcanoclastic flysch, and oceanic basalts	Greenschist-blueschist	Glaucophanic greenschist, mélange, and flysch and basalt	99CH2; 01CH8, 10, 22, 45, 47, 48, 49
Ghost Rocks	Accreted by 62 Ma	Early Paleocene andesite, pillow basalt, deformed sedimentary units, and pelagic limestone	Prehnite-pumpellyite	Also considered to be a formation included with the Prince William terrane	None (Offshore, west of study area)
Prince William	Accreted by 51 Ma	Flysch complex, marine volcanic rocks, and hemipelagic mudstone; also ophiolites and turbidites	Zeolite to greenschist	<i>Orca Group</i> ; also <i>Resurrection Peninsula Sequence</i> and <i>Sitkalidak Formation</i>	99CH1; 01CH26, 28
Yakutat	~30 Ma to Present	<i>West of Dangerous River Zone</i> : Paleocene to Eocene oceanic basalt overlain by siliciclastic units <i>East of Dangerous River Zone</i> : Upper Mesozoic flysch and mélange and Tertiary intrusive rocks overlain by clastic sediments	Greenschist	<u>Paleocene to early Oligocene</u> <i>Hubbs Creek basalt</i> <i>Oily Lake siltstone</i> <i>Tokum and Stillwater Fms.</i> (slope and shelf deposits) <i>Kulthieth Fm.</i> (shallow marine and nonmarine units) <u>Late Eocene to early Miocene</u> <i>Poul Creek Fm.</i> (argillaceous sediments with interbeds of basaltic tuff, breccia, and pillow basalt) <u>Middle Miocene to Present</u> <i>Yakataga Fm.</i> (Siliciclastic sed. with glacial material) <i>Redwood Fm.</i> (Siliciclastic sed. without glacial material)	01CH29, 34, 38, 39, 41, 43, 56; 02CH28, 31, 32

Table 2.1

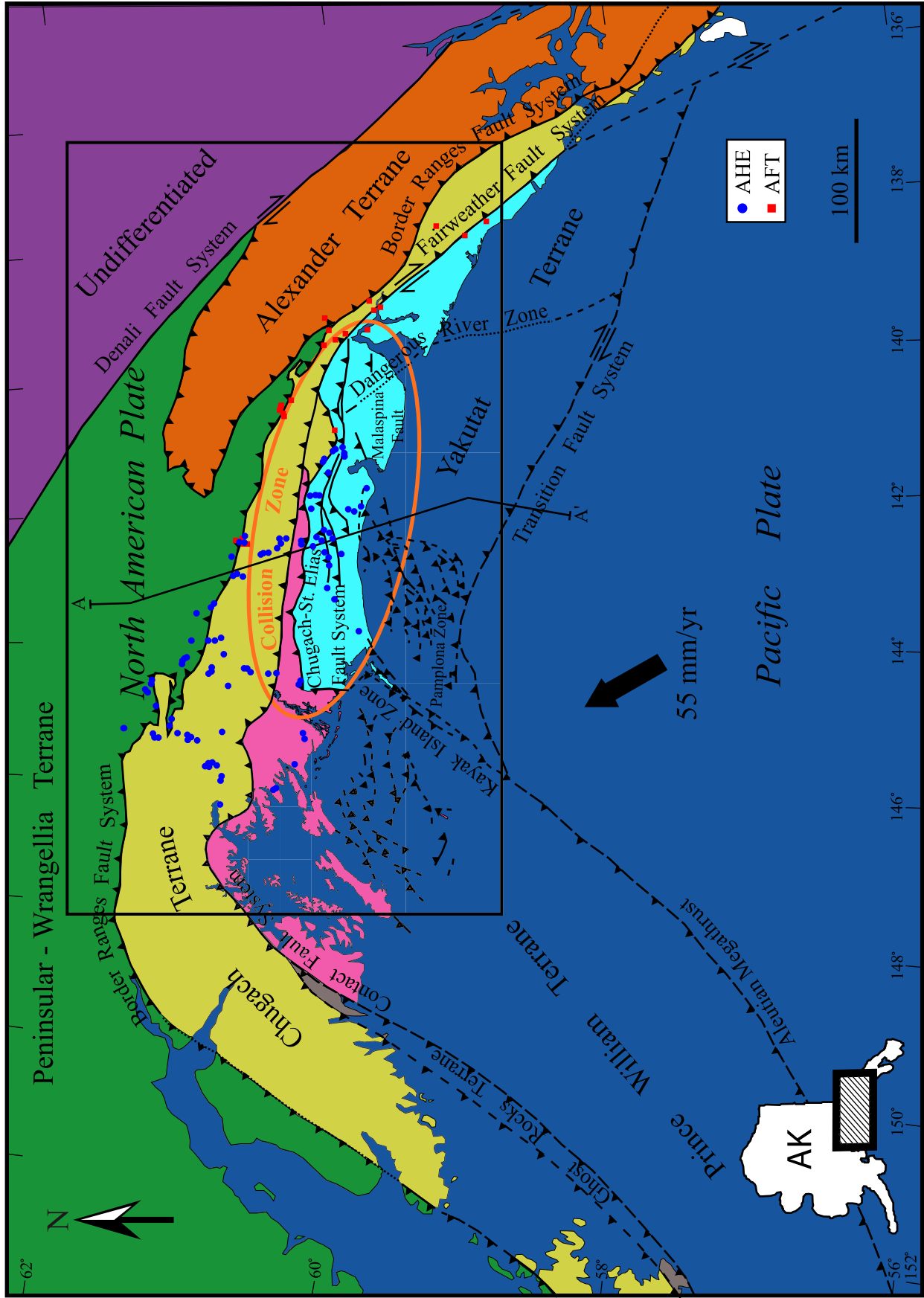


Figure 2.1

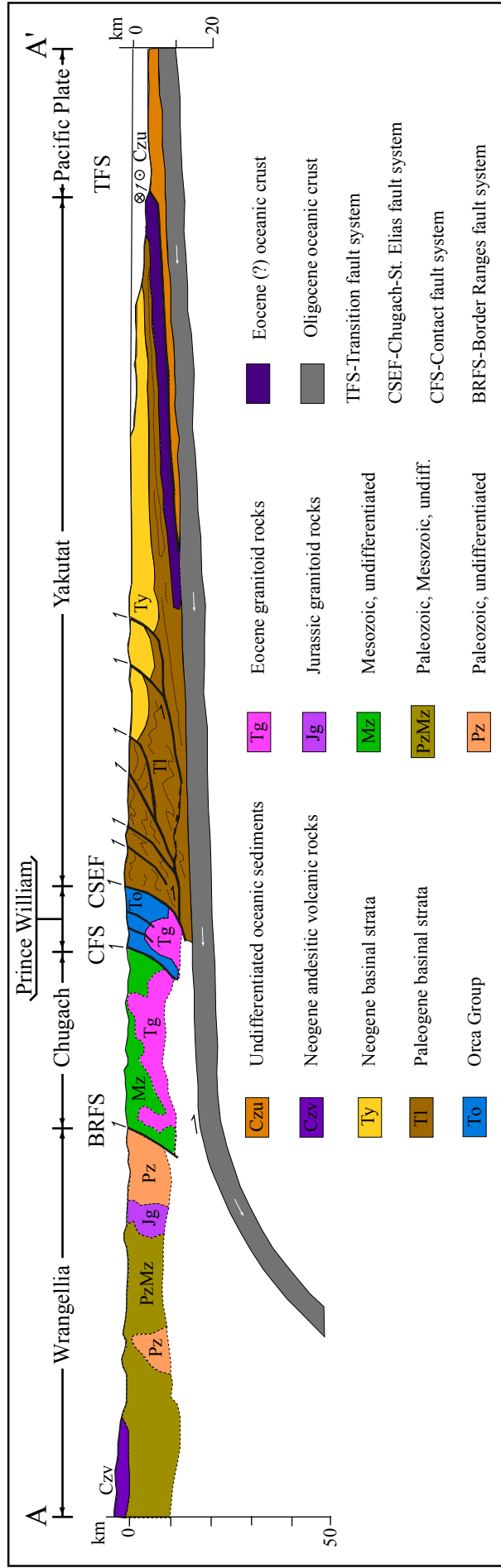


Figure 2.2

Figure 2.3



2.2 Late Cenozoic Glacial and Sedimentation History

Glacially-sculpted mountains typical of high latitudes illustrate how effectively glaciers transform topographic surfaces (Figure 2.4). To understand the role of glaciers, long-term exhumation rates must be quantified using thermochronology. However, the sedimentary record and regional climate change provide important constraints on the timing of glaciation and sediment yields over different time scales. Late Cenozoic sediments in fjords, on land, and on the shelf provide a rich record of the glacial and tectonic history of the CSEM. The sedimentation history and the pattern of glaciation in space and time in the CSEM are discussed below.

High maritime precipitation originating from the Gulf of Alaska has been trapped by the towering CSEM and stored as valley glaciers for most of the history of uplift over the past 5 Myr (Figure 2.5) (Lagoe et al., 1993; Jaeger et al., 1998; Meigs and Sauber, 2000). The northward progression of storms into the range has produced a disproportionate glacier distribution across strike (Figure 2.6). Major piedmont glaciers, including some of the largest glaciers in North America (Bagley Icefield, Bering Glacier, and Malaspina Glacier), occur along the windward side of the range, whereas small, isolated glaciers cling to the upper reaches of the northern flanks of the range (Figure 2.7) (Jaeger et al., 1998; Meigs and Sauber, 2000). This pattern is represented by the northward increase in equilibrium line altitude (ELA), the boundary that distinguishes a glacier's zones of accumulation and ablation (Figures 2.6 and 2.8). ELA correlates well with precipitation, with the highest amount of rain and snow occurring along the coast (>2-3 m/yr according to Jaeger et al., 1998) (Figure 2.9) (Meigs and Sauber, 2000).

During the last glacial maximum, ELA on the southern flank of the range was at least 800 m below present day elevations, while ELA on the northern flank dropped by only 100-200 m (Péwé, 1975; Meigs and Sauber, 2000). The significant drop in ELA on the windward side of the range increased landscape area in the accumulation zone by as much as ~75-95%, allowing large coastal glaciers to form during the last glacial maximum (Péwé, 1975). For example, glacier terminus and trimline locations indicate that ice covered ~64% of a 4 km-high wall of Taan fjord in Icy Bay in 1900 A.D., when the glacier terminus was at the modern coastline and the bay was ice-covered (Porter, 1989a; Paterson, 1994). During the last glacial maximum, the entire wall of Taan fjord was ice-covered. Landward movement of the Tyndall glacier terminus more than 20 km from the modern coastline since 1900 A.D. reflects rapid glacier retreat typical of southern Alaska over the last few hundred years.

The glaciation of the CSEM over the last 5-6 Ma is represented by sedimentology and fossils in the siliciclastic, glacially-derived, 5000-m thick late Cenozoic Yakataga Formation exposed along coastal portions of the range (Plafker, 1987; Lagoe et al., 1993; Plafker et al., 1994b). The Yakataga Formation contains the best late-Cenozoic record of glaciation in the northern latitudes and is located stratigraphically above the Poul Creek Formation throughout the Yakutat terrane (Table 2.1 and Figure 2.10) (Lagoe et al., 1993). As summarized by Lagoe et al. (1993), the boundary between early Miocene chalk deposits, which contain little terrigenous sediment, and fan deposits at 5-6.7 Ma is believed to mark the emergence of the coastal CSEM and the first occurrence of glacial diatom biofacies. The first planktic foraminifera attributed to subarctic climates are found above ice-rafted debris in the upper Poul Creek Formation and can be correlated to a magnetostratigraphic age of approximately 5.35 Ma near the Poul Creek/Yakataga contact. A decrease in glaciation during the mid-Pliocene, inferred by changes in foraminifera coiling direction and $^{18}\text{O}/^{16}\text{O}$ ratios, was followed by a significant increase in ice-rafted debris between 3.5 and 2.48 Ma. The association of glacial fauna with uplift of the coastal mountains throughout the Yakutat terrane suggests that the changing topography of the CSEM, in conjunction with global climate change, have influenced climatic patterns to create the modern distribution of glaciers.

The effects of short-term glacial erosion on the CSEM can be inferred by sediment deposition on the continental shelf and in tidewater fjords from the Holocene to the present. 100-year depositional rates were determined for sediment cores from the continental shelf by calculating the exponential decay of ^{210}Pb activity since burial (Jaeger et al., 1998). High sediment accumulation rates over 100-year time scales on the western side of Kayak Island (>10 mm/yr), near the entrance of Prince William Sound southwest of Hinchinbrook Island (>20 mm/yr), and seaward of the Copper River Delta (>20 mm/yr), are associated with westward marine transport of sediment generated from the Bering Glacier, Malaspina Glacier, and Copper River (Figure 2.7). An average depositional rate of 7.9 mm/yr over Holocene time scales is inferred for the continental shelf between Icy Bay and Cross Sound, southeast of the Alsek River (Sheaf et al., 2003). Jaeger et al. (2002) determined that the effective erosion rates (inferred removal rates of crystalline material from the orogen based on accumulation rates) over the past 100 years are ~1-2 mm/yr for the entire Gulf of Alaska, and 1.0, 2.5, and 3.0 mm/yr for the Copper River, Bering, and Malaspina Glaciers, respectively. Holocene rates were determined by

estimating the depth to a seismic reflector inferred to be the Holocene boundary. Estimating seismic velocities for shelf sediments and using the seismic reflector as a marker for Holocene glaciation may have exaggerated Holocene rates. Effective erosion rates over Holocene time scales are 5.1 mm/yr for the Gulf of Alaska adjacent to the St. Elias Mountains (Sheaf et al., 2003) and 1.5, 3.5, and 5.0 mm/yr for the Copper River, Bering, and Malaspina glaciers, respectively (Jaeger et al., 2002).

Sediment trapped in fjords proximal to glaciated areas accounts for a significant amount of glacial outwash that is not represented by 100-year data from shelf deposits (Figure 2.11) (Hallet et al., 1996; Jaeger et al., 1998). Effective erosion rates for selected southeastern Alaska fjord basins average 10s of mm/yr for time spans of a few years to 100s of years and are among the highest ever measured in the world (Hallet et al., 1996). Basins with >30% glaciers have sediment yields that are approximately one order of magnitude greater than non-glaciated basins. High effective erosion rates inferred from fjord sedimentation are widely accepted as evidence for the efficiency of glacial erosion, but fjord geometry, sediment recycling, and sporadic glacial surges limits the ability of assigning high rates entirely to short-term glacial denudation (Hallet et al., 1996; Jaeger et al., 1998). Koppes and Hallet (2002) attributed high sediment yields in fjords to rapid glacial retreat after the Little Ice Age period ended approximately 200 years ago. If fjord sedimentation reflects short-term fluctuations of the glacial-interglacial cycle, then it becomes difficult to assign high effective erosion rates to long-term glacial erosion.

Figure Captions

Figure 2.4 Narrow ridges, U-shaped valleys, and large moraines located in the northern Chugach Mountains between samples 02CH26 and 02CH27 illustrate how glaciers can impact landscape development, even on the leeward side of the range.

Figure 2.5 Large glaciers are focused near high peaks of the Chugach-St. Elias Mountains. Glacial extent is outlined in yellow and overlays a shaded-relief map that displays elevation. The yellow dots are AHE sample locations. Shaded relief map was created in ArcMap using a 60 m grid digital elevation model (DEM) from the U.S.G.S.

Figure 2.6 Schematic diagram of across-strike glacier distribution for the Chugach-St. Elias Range. ELA data from Meigs and Sauber (2000) and Easterbrook (1999). Geologic units based on data from Plafker (1987) and Plafker et al. (1994b). Precipitation data from Jaeger et al. (1998).

Figure 2.7 Glacier distribution in Chugach-St. Elias Mountains.

Figure 2.8 Northward increase in ELA reflects a northward decrease in glacial coverage. ELA contour map from Meigs and Sauber (2000).

Figure 2.9 A negative correlation is evident between ELA and precipitation. Modern ELA steadily increases northward while precipitation drops off significantly north of the Chugach-St. Elias Mountains. ELA and precipitation data from Meigs and Sauber (2000).

Figure 2.10 Inferred timing of glacial activity based on sedimentary units from the Yakataga and Poul Creek formations. The presence of glauconite in the Poul Creek formation reflects decreased sediment accumulation, and the abrupt introduction of ice rafted debris in the Yakataga formation marks the onset of glaciation in the region. Fluctuating glacial activity is also inferred from the varying amount of ice rafted debris in the Yakataga formation. Figure based on glacial data from Lagoe et al. (1993) and formation and unit data from Plafker (1987), Lagoe et al. (1993), and Plafker et al. (1994b).

Figure 2.11 Sediment yields from glacially-dominated orogens of southern Alaska are greater than glacial and fluvial yields from the rest of the world. Figure is synthesis of data from Hallet et al. (1996).

Figure 2.4



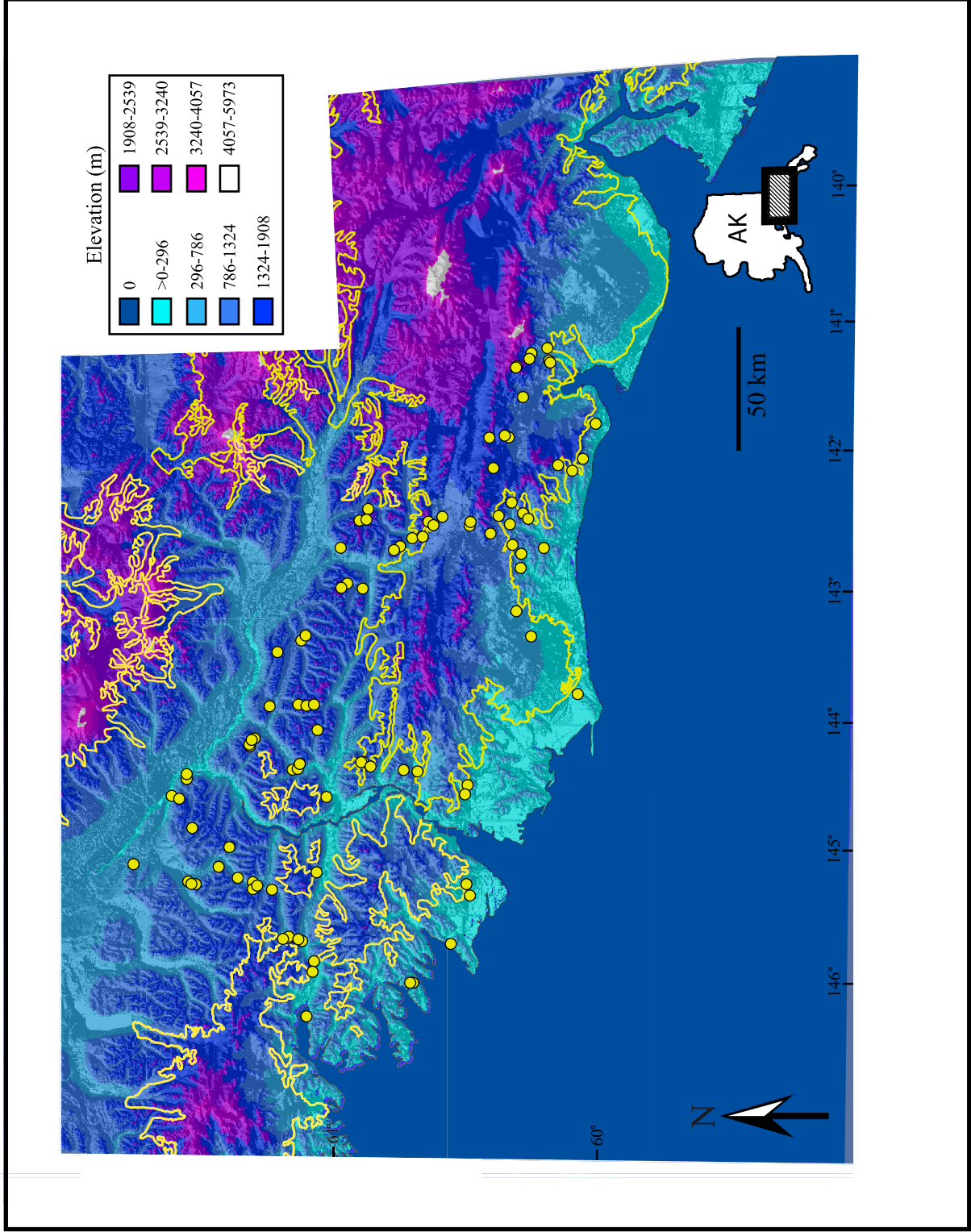


Figure 2.5

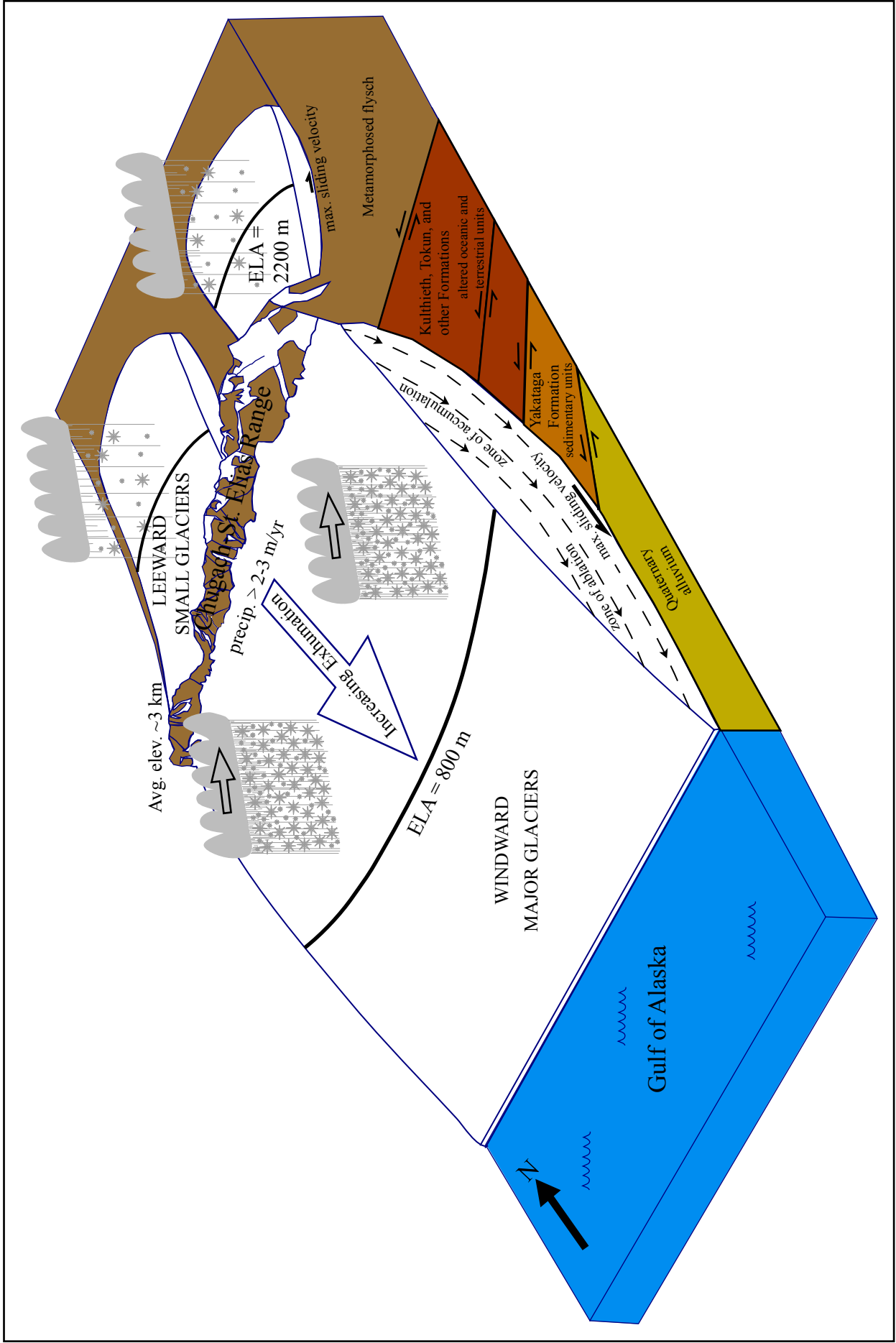


Figure 2.6

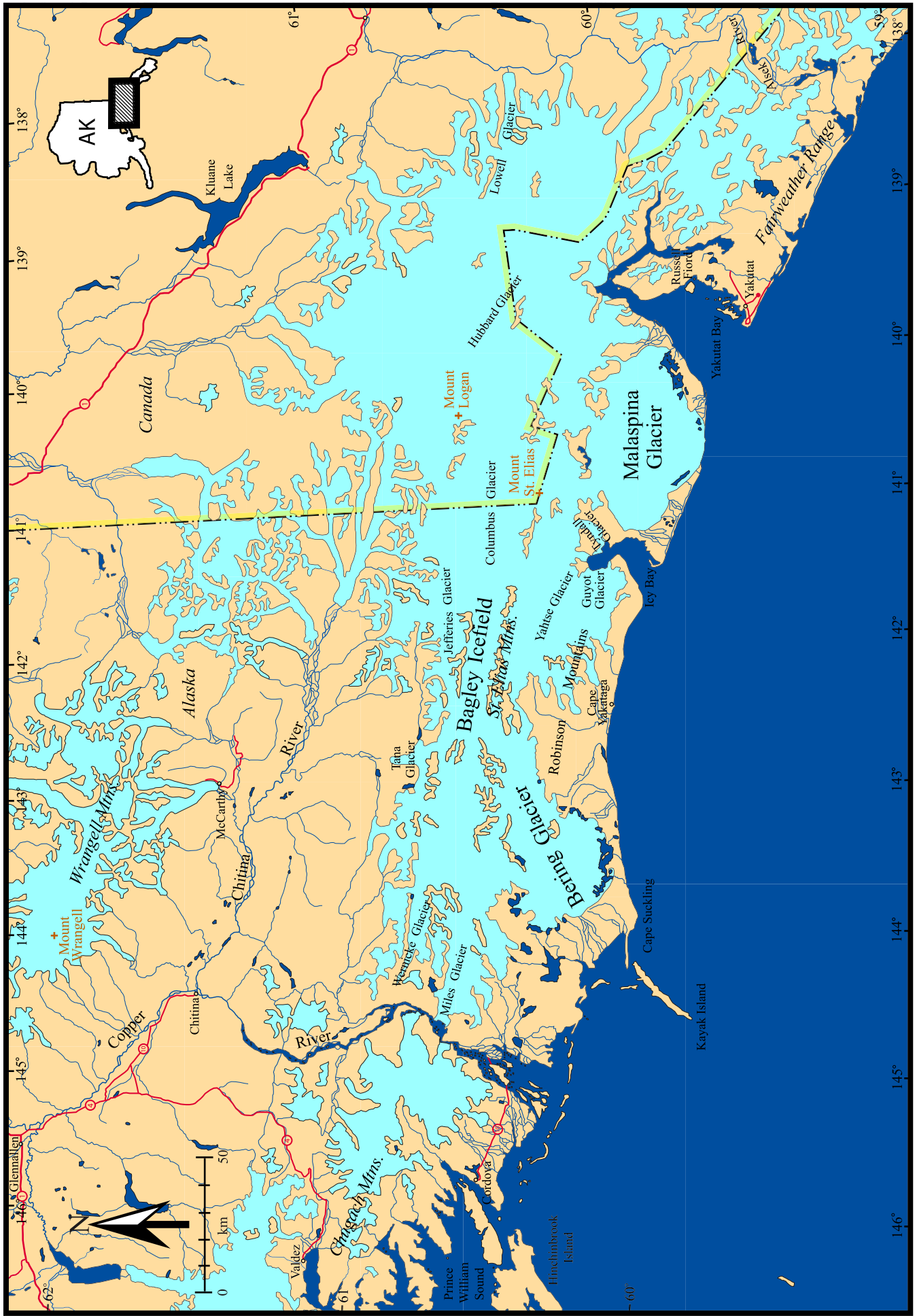
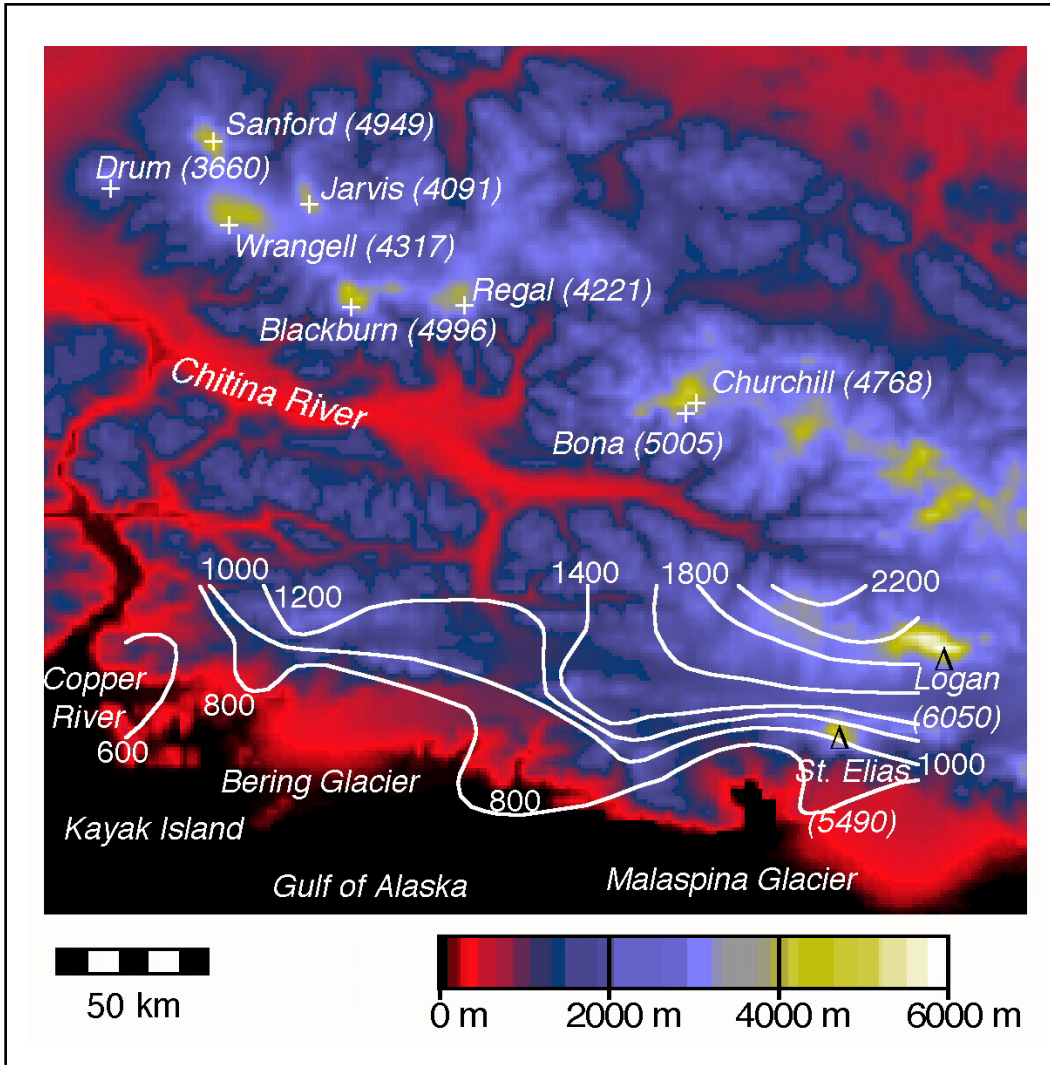


Figure 2.7

Figure 2.8



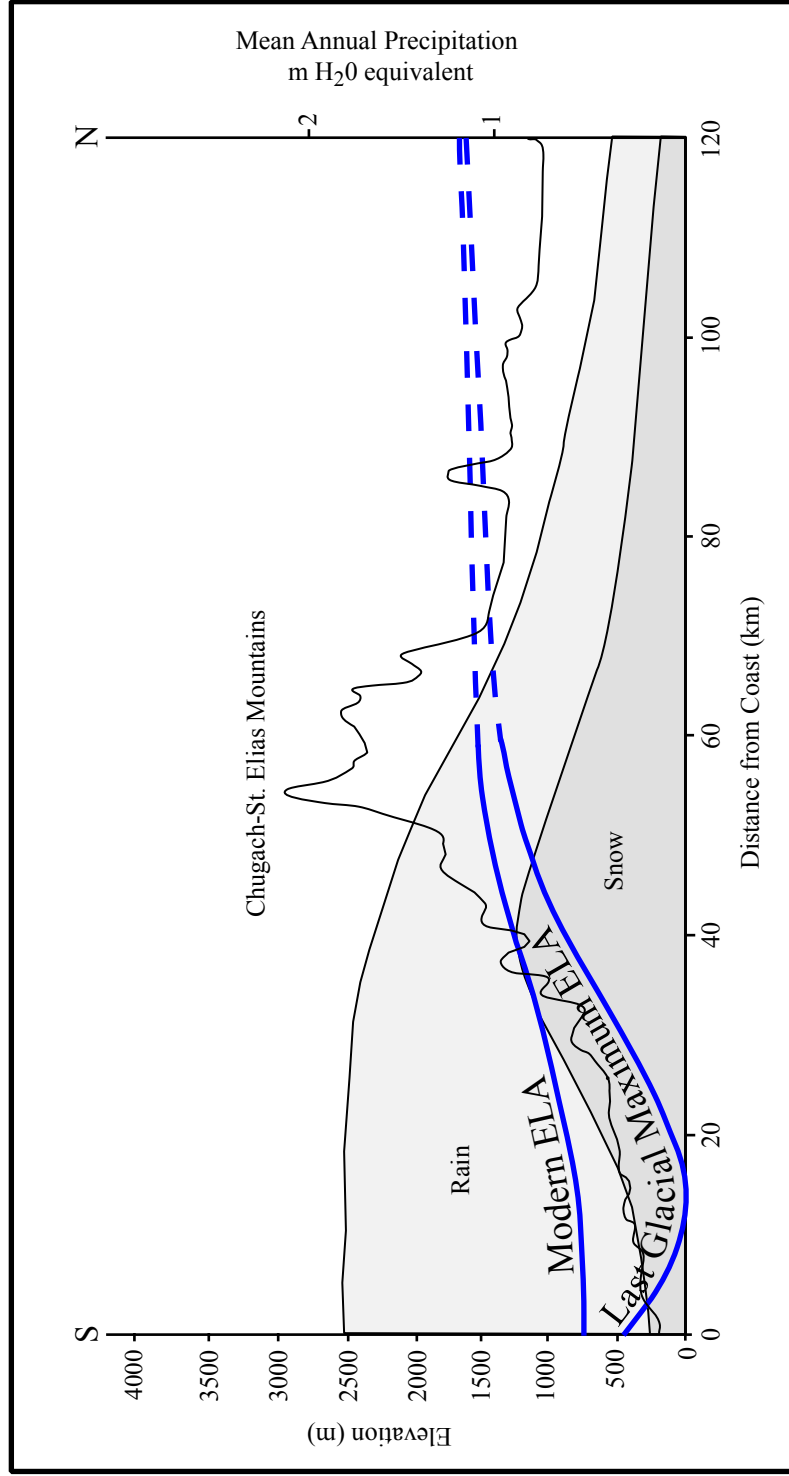
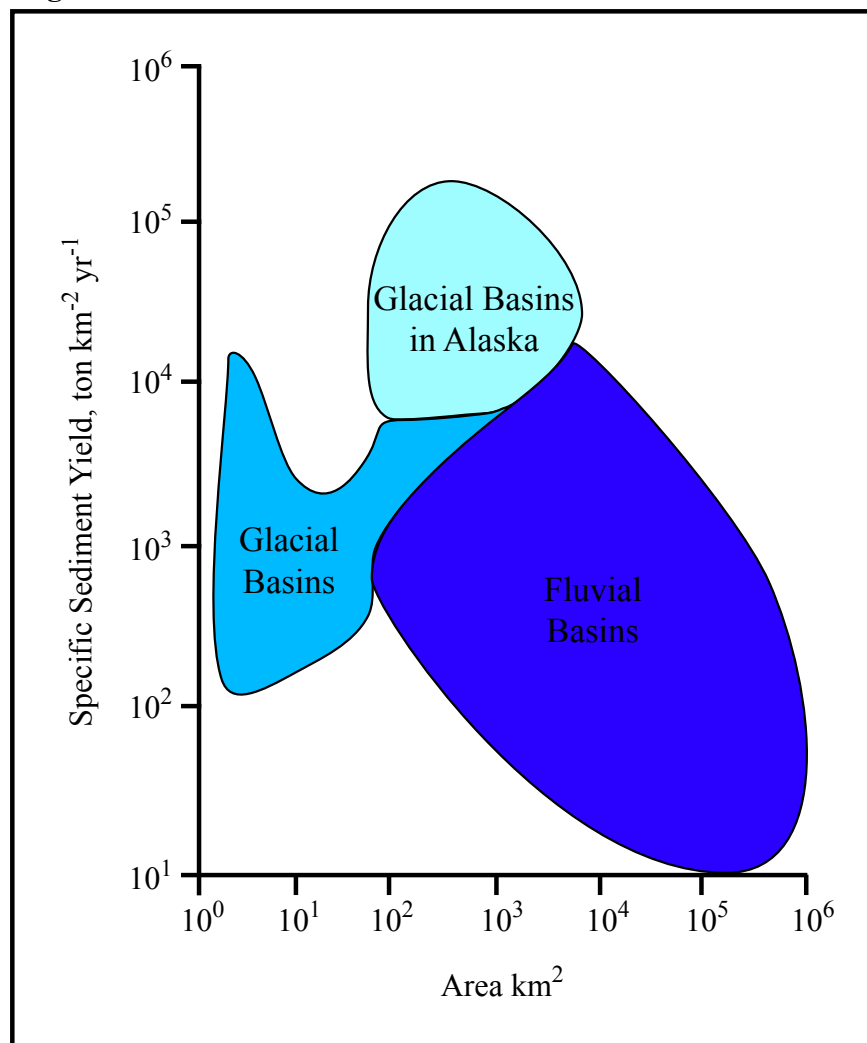


Figure 2.9

Figure 2.10

EPOCH	FORMATION	INFORMAL UNITS	GLACIAL ACTIVITY
Pleistocene	Yakataga Thickness of ~5000 m	Upper Glaciomarine Unit	Intense Glaciation ~3.0 Ma to Present
Pliocene		Normal Marine Unit	Warming Period ~4.2 to 3.0 Ma
		Lower Glaciomarine Unit	Glaciation Begins ~6.7-5.0 Ma
Miocene	Poul Creek Thickness of ~2000 m	Glauconitic Clastic Unit	
		Regional Hiatus	
		Organic Shale	
Oligocene		Argillaceous Clastic Unit	

Figure 2.11



2.3 Apatite Fission Track (AFT) Data

The long-term exhumation history of a mountain range is recorded by low-temperature thermochronometers. The apatite fission track (AFT) technique evaluates lengths and annealing properties of fission tracks attained at temperatures between 60°C and 110°C to acquire a shallow-crustal residence age (O'Sullivan et al., 1997). Each age can be used with the sample closure temperature and a presumed geothermal gradient to determine an exhumation rate. The spatial distribution of dated samples can be used to constrain regional exhumation rates related to tectonic and glacial activity. Minimal work has been done for the CSEM, but a few AFT studies in the St. Elias Mountains and in the Mt. Logan area provide some constraints of exhumation (Figure 2.12) (Long, 1992; O'Sullivan and Currie, 1996; O'Sullivan et al., 1997).

AFT ages from the eastern St. Elias Mountains and Fairweather Range are young. Ages decrease roughly to the southeast, from 4.5 ± 0.9 Ma north of Yakutat Bay to 1.3 ± 0.3 Ma just south of the Alsek River (O'Sullivan et al., 1997). The southeastward decrease in age along strike does not follow primary metamorphic gradients created by Miocene igneous intrusions, and there is little variation in age across major fault and terrane boundaries (O'Sullivan et al., 1997).

AFT ages from a vertical profile of the Mt. Logan area are old to young depending on elevation (O'Sullivan and Currie, 1996). Samples are 40 ± 5 Ma near the top of Mt. Logan at elevations of ~ 5000 m and 4 ± 1 Ma for base elevations of ~ 2000 m. A comparison of age and track length with elevation for the massif shows three abrupt changes in slope indicative of increased denudation over the last 40 Ma. AFT samples from a different study in the interior of the St. Elias Mountains, north of the Bagley Icefield, have ages that are comparable to higher elevation samples from Mt. Logan (26-40 Ma) but are ~ 4 km lower in elevation (Long, 1992).

The sparse distribution of AFT samples in such a small area of the eastern St. Elias Mountains limits the understanding of exhumation for the region (O'Sullivan et al., 1997). Ages decrease to the southeast along the Fairweather and Boundary faults, but there is no correlation between age distribution and fault locations. If ages are used to infer exhumation rates, then the southeastward decrease in age indicates that rates increase to the southeast away from the syntaxial bend, contrary to an expected decrease in rates away from the deformation front. The exhumation rate inferred from an age-elevation plot for all of the samples ranges from 1.5-1.9

mm/yr, but large horizontal distances between these samples limits the use of this plot as a vertical profile.

The vertical profile from the Mt. Logan area demonstrates that exhumation rates have varied over the last 40 Ma (O'Sullivan and Currie, 1996). The inferred exhumation rates from the three abrupt denudation events are 0.7 mm/yr for post-Eocene cooling, 0.3 mm/yr for the mid-Miocene and 0.3 mm/yr for the Pliocene. There is no direct correlation between these events and regional tectonic activity, so it is unclear what triggered the onset of denudation. The correlation between ages from Mt. Logan and ages from the interior of the St. Elias Mountains (Long, 1992) indicates that exhumation was similar between both areas, but the location of samples ~4 km higher at Mt. Logan indicates that exhumation increased in the Mt. Logan area after ages were set.

The lack of a correlation between exhumation patterns and major tectonic boundaries is established by AFT ages, but the location of these samples outside the core of the collision zone limits the understanding of how active tectonics is affecting landscape evolution. The northward increase in fault dip within the core of the collision zone to the west of the AFT sample locations is believed to create a distinct exhumation pattern and rates that are higher than those reported by AFT.

Figure Caption

Figure 2.12 AFT sample locations. Samples located in the interior of the St. Elias Mountains are from Long (1992), Mt. Logan samples are from O'Sullivan and Currie (1996), and those in the eastern portion of the range are from O'Sullivan et al. (1997).

CHAPTER 3: METHODS AND RESULTS

3.1 Apatite Radiogenic Helium (AHE) Technique

Geologists have traditionally relied on empirical evidence and numerical models to determine how rocks are exposed at the earth's surface. The rediscovery of the apatite radiogenic helium ([U-Th]/He or AHE) technique has revolutionized the understanding of landscape development by enabling rock exhumation to be quantified (Zeitler et al., 1987; Lippolt et al., 1994; Wolf et al., 1996; Warnock et al., 1997; Reiners and Farley, 1999). Apatite grains retain helium at temperatures lower than ~70-90°C, allowing an age to be determined for the time rocks move through shallow crustal levels (Wolf et al., 1996). The AHE technique has the lowest closure temperature of any thermochronometer, including apatite fission track dating (~100°C), making it the most sensitive tool for estimating exhumation from shallow crustal levels (Ehlers and Farley, 2003).

3.1.1 Helium diffusion and measuring exhumation

The AHE technique measures the accumulation of alpha particles (⁴He) in apatite grains produced by the decay of U and Th isotopes. The concentration of parent isotopes and the amount of retained α (daughter) particles is used to determine the helium age by solving for (t) in the following equation,

$${}^4\text{He} = 8({}^{238}\text{Ab})({}^{238}\text{U})(e^{\lambda t}-1) + 7({}^{235}\text{Ab})({}^{235}\text{U})(e^{\lambda t}-1) + 6({}^{232}\text{Ab})({}^{232}\text{Th})(e^{\lambda t}-1)$$

where Ab = natural abundance of isotope, U = amount of uranium, Th = amount of thorium, λ = decay constant, and t = time (Wolf et al., 1998; Ehlers and Farley, 2003). Assuming a typical geothermal gradient of ~25°C/km, a “helium age” represents the time of exhumation from ~1-3 km depth (Wolf et al., 1998; Ehlers and Farley, 2003). Since thermally-controlled helium diffusion is partial in the temperature range of ~40-80°C, a helium partial retention zone (HePRZ) exists at depth. The HePRZ defines a transitional depth range where helium accumulates at a variable but partial rate (Figure 3.1) (Wolf et al., 1998; Ehlers and Farley, 2003). The longer a sample spends in this zone, the lower its closure temperature (T_c), such that closure temperature is correlated with cooling rate.

3.1.2 Helium dating procedures

The initial step in acquiring a sample age was to extract and measure trapped helium in apatite grains using the vacuum extraction line at Virginia Tech. Aliquots of 15-20 grains were placed in steel capsules or platinum tubes and heated to temperatures in excess of 900°C to drive

off retained helium. The liberated gas was sent to a cryogenic trap that separates helium from impurities in the line. The purified helium was combined with a ^3He spike of a known concentration and sent through a quadrupole mass spectrometer, where $^4\text{He}/^3\text{He}$ ratios were measured and compared to known standards to determine the number of ^4He atoms outgassed. After complete degassing, grains were analyzed for U and Th concentrations. Samples were removed from the helium line and the outgassed grains were dissolved in nitric acid. A known concentration of U and Th was added to the solution and the sample was analyzed by isotope dilution using inductively coupled plasma mass spectrometry (ICP-MS) at either 1) ACTLABS in Ontario, Canada, 2) Yale University, or 3) California State University, Bakersfield, depending on time of measurement.

Helium diffusion is partly dependent on grain size, because the diffusion domain is the apatite crystal itself (Farley, 2000). T_c is also affected by grain size where an increase in crystal width from 50 to 150 μm increases T_c by $\sim 10^\circ\text{C}$. Helium ages must also be corrected for alpha ejection. Alpha particles ejected from U and Th nuclides have average stopping distances of $\sim 20 \mu\text{m}$. Since helium produced near the surface of a crystal may be lost, measured helium ages are too young unless ejection is corrected for. The correction factor for helium retentivity (F_T) was determined by first calculating the surface area to volume ratio of each grain using length/width measurements and then by using the grain dimensions in an expression that relates ^{238}U series retentivity with a model cylindrical shape (Farley et al., 1996). To ensure that ages were not artificially low, the dimensions of each grain were carefully measured with a binocular microscope and the corresponding helium retention (F_T) value was used to correct the raw helium age. The uncertainty of whether the emission source was generated from within the interior of the crystal or along the edge required apatite grains to be at least 60 μm in width to have a representative amount of helium. Apatite grains that have U and Th mineral inclusions can contain extraneous alpha particles (House et al., 1997). Zircon, monazite, and xenotime inclusions commonly found in apatite tend to have high U and Th concentrations, which increase the amount of retained daughter particles and create artificially high helium ages. Zoning created by the arbitrary distribution of U and Th also introduces errors, but running multiple aliquots for each sample usually helps sort out chemical inconsistencies (Ehlers and Farley, 2003). To avoid erroneous ages, samples were screened for inclusions with a binocular microscope using crossed

polars. Grains with high birefringent spots, poor shape, severe mottling, or any bright inclusions were not analyzed.

Apatite was extracted from granitic, sedimentary, and metasedimentary rocks using heavy liquids and magnetic separation at Apatite to Zircon, Inc. in Viola, Idaho. The commonness of apatite allows grains to be found in almost any rock type, but obtaining large, flawless grains that can be analyzed by the AHE technique is difficult. Granodiorites and tonalites typically yield large, euhedral grains with a low occurrence of inclusions, while volcanic, sedimentary, and metasedimentary rocks usually yield small, anhedral to subhedral grains with numerous inclusions. The predominance of metasedimentary rocks throughout our sample collection has drastically limited the amount of usable grains for helium dating (Table 3.1). A number of grains were small with poor shape, severely mottled, and littered with inclusions. Screening for usable grains was the limiting factor in producing helium ages.

3.1.3 Helium age uncertainties

Sample errors produced from analytical measurements, age reproducibility, and low gas concentrations ranged from 10-30% (Table 3.2). Grain measurements, F_T corrections, vacuum extraction line procedures (addition of ^3He spike, accelerated heating gradients relative to natural cooling conditions), ICP-MS procedures, and reproducibility of the Durango standard age at the Virginia Tech facility are assumed to have contributed errors that total $\pm 10\%$ for each sample. Samples that yielded low gas concentrations (due to small grain mass and/or young age) close to line-blank levels had errors of $\sim 30\%$, based on the sensitivity of age determinations to minor line-blank corrections. Intermediate uncertainties were also assigned in case of low He content or low U/Th concentrations.

The poor quality of apatite grains from the CSEM is the primary cause for high helium age errors. Rocks that contained only trace amounts of apatite and yielded only small crystals produced little helium that was barely detectable above line-blank levels. Samples located close to the Alaska coast that yielded small apatite grains produced almost undetectable amounts of helium because of localized rapid cooling rates.

3.1.4 Sample collection strategy

Samples were collected along strike of the CSEM from Valdez to Icy Bay and across strike from the coast to the Chitina River valley, to constrain long-term exhumation rates and determine large-scale effects of glacial erosion (Figure 3.2). Our primary objectives were to

collect enough samples to properly represent the varying glacial and tectonic features throughout the range and to analyze rock types that typically yield high-quality apatite grains to reduce dating errors. The rugged terrain and predominance of poor-quality apatite-bearing rocks throughout the CSEM dramatically limited our selection of sample locations. Several locations were chosen based on helicopter accessibility or desired rock type (granites and gneisses that yield high quality apatite grains), although many samples known to yield poor-quality grains were collected based on the strategic location near critical glacial, tectonic, or vertical elevation controls (Icy Bay area; west of Copper River).

A total of 97 samples were collected primarily by helicopter throughout the CSEM in the summers of 1999, 2001, and 2002 (Figure 3.2). These consist of metasedimentary rocks (schist and phyllite), with a minor amount of sandstone, granodiorite, gneiss, and volcanic rocks. Rugged terrain and extensive glacial coverage limited rock collection to ridge tops for many samples (Figure 3.3). Four across-strike profiles (AA'-DD') were created to compare the variations between glacial coverage, tectonic setting, and sample elevations (Figure 3.2). Samples along AA' and BB' are located in a less glaciated region of the CSEM within the hanging wall of the Aleutian trench away from the deformation front. Samples along CC' and DD' are located in a heavily glaciated region within the hanging wall adjacent to the deformation front of the underthrusting and accreting Yakutat terrane. Samples collected along the northern extent of profile BB' and north of Icy Bay near DD' were analyzed to establish age-elevation relationships. A total of 53 samples weighing 5-10 kg each have been processed for mineral separation by Apatite to Zircon, Inc. in Viola, Idaho, over the past two years; 4 samples from the 1999 field season, 36 samples from 2001, and 13 samples from 2002. Additional samples have been curated at Virginia Tech.

Figure Captions

Table 3.1 Location and lithology of samples analyzed by AHE. Apatite grains were judged as good, fair, or poor based on the predominance of inclusions, small grain sizes, and small grain yields.

Figure 3.1 Age and temperature variations in the helium partial retention zone (HePRZ). A sample will acquire a higher helium age if it spends a longer time in the HePRZ (Wolf et al., 1998).

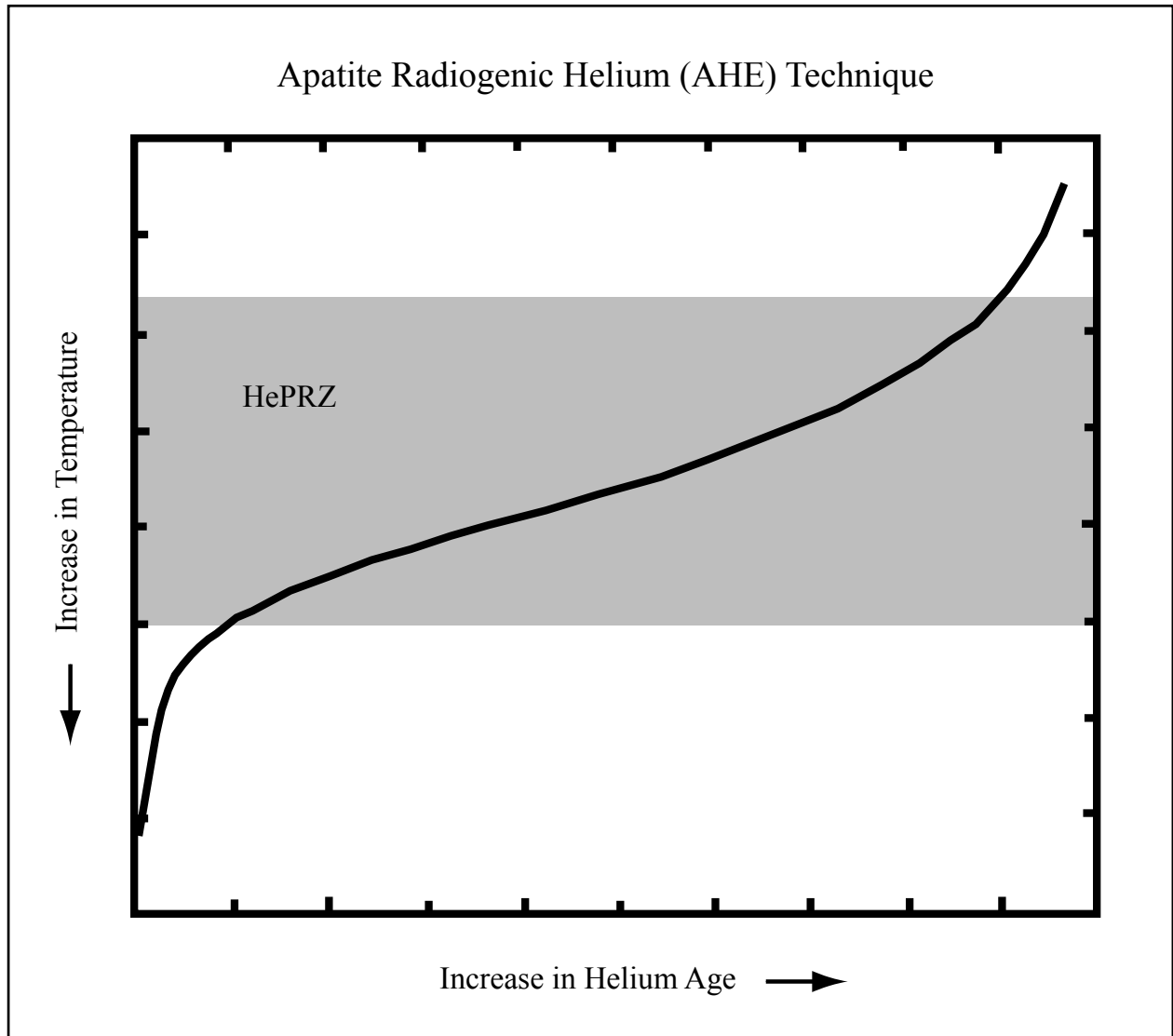
Figure 3.2 AHE and AFT sample locations. Dated samples are represented by squares and undated samples by circles. Profiles AA'-DD' are shown in Figure 3.5. AFT samples are from Long (1992), O'Sullivan and Currie (1996), and O'Sullivan et al. (1997). Tectonic data from Plafker (1987) and Plafker et al. (1994b).

Figure 3.3 Samples were typically collected along ridges between glaciers due to limited accessibility, as is shown for 01CH55 located east of the Tyndall glacier.

Table 3.1

Sample	Profile	Elevation (m)	Distance From Coast (km)	Rock Type	Apatite Quality
99CH1	BB'	46	15.3	granodiorite	fair
99CH2	CC'	754	72.8	gneiss	good
01CH4	AA'	1417	112.2	metagraywacke	poor
01CH8	AA'	1174	90.3	metagraywacke	poor
01CH10	AA'	671	49.1	schist	poor
01CH22	BB'	1532	82.7	schist	fair
01CH26	BB'	884	37.5	granite	poor
01CH28	BB'	564	18.6	granite	good
01CH29	CC'	1082	27.4	sandstone	fair
01CH34	CC'	579	16.3	sandstone	fair
01CH38	CC'	640	23.5	graywacke	fair
01CH39	CC'	297	15.8	graywacke	poor
01CH41	DD'	274	6	graywacke	fair
01CH43	DD'	279	35.1	graywacke	good
01CH45	CC'	1783	66.6	granite	fair
01CH47	CC'	1494	77.2	schist	fair
01CH48	CC'	1920	79.4	schist	poor
01CH49	CC'	2012	68.1	schist	poor
01CH56	DD'	1135	43.4	graywacke	poor
02CH1	BB'	1829	127.8	diorite	good
02CH2	BB'	1524	128.6	diorite	good
02CH3	BB'	1074	127.7	phyllite	poor
02CH4	BB'	1259	128.7	diorite	good
02CH19	CC'	1402	105.3	diorite	good
02CH28	DD'	1625	43.1	graywacke	poor
02CH31	DD'	1387	39.6	graywacke	fair
02CH32	DD'	1478	39.1	graywacke	fair

Figure 3.1



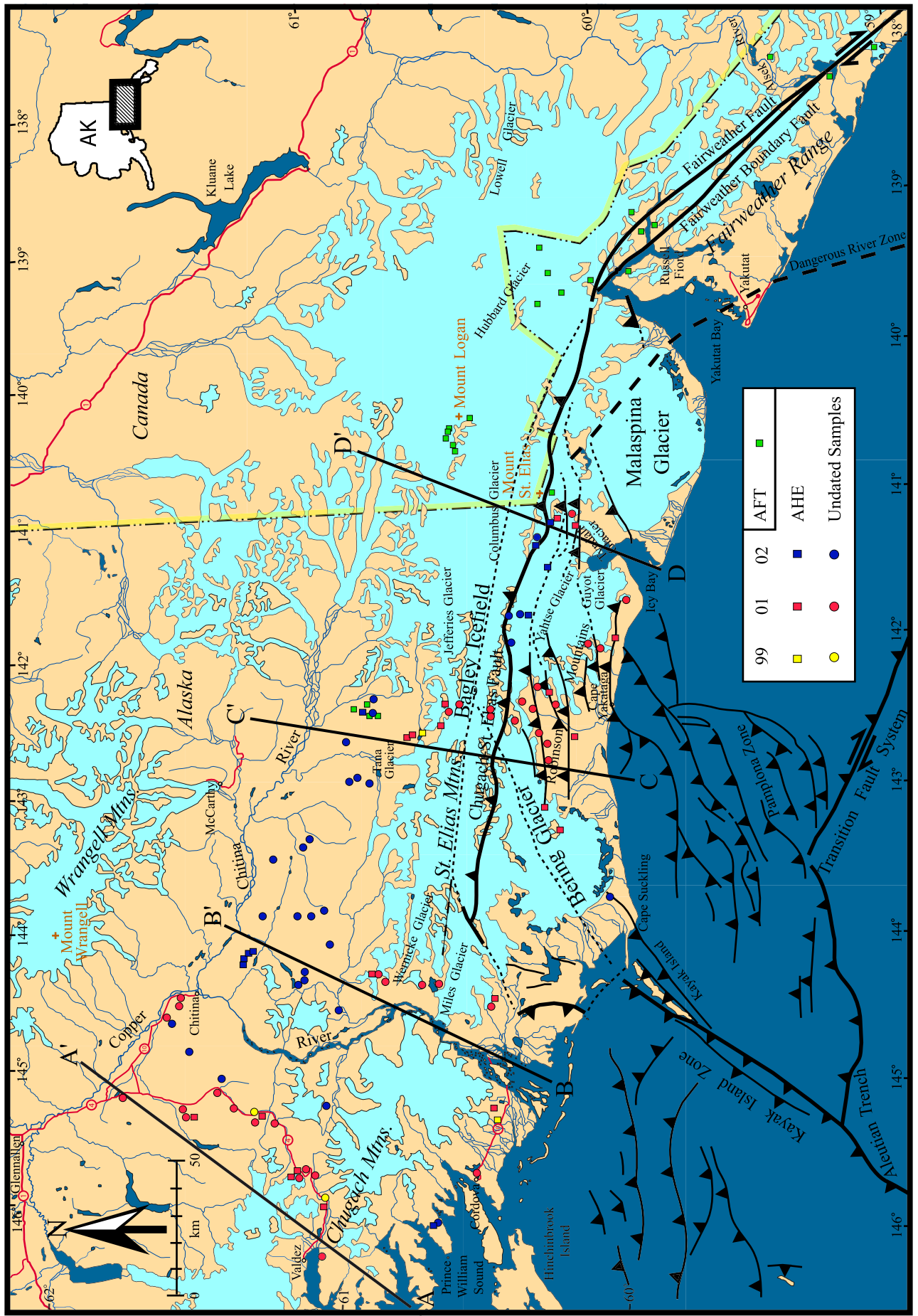
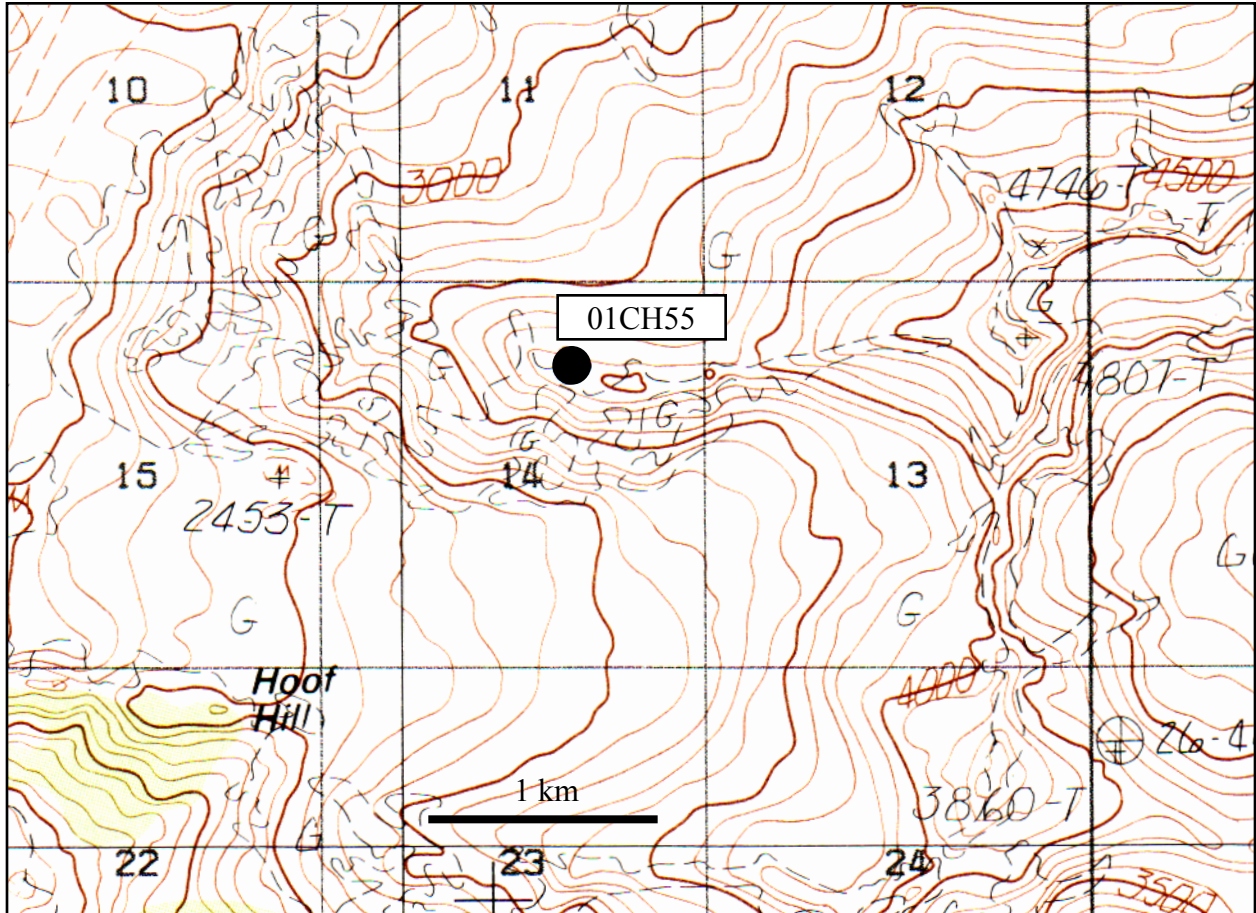


Figure 3.2

Figure 3.3



3.2 Results

A total of 27 samples collected both along and across the strike of the CSEM have been analyzed using the AHE technique. Ages are plotted on maps and elevation profiles in Figures 3.4 and 3.5, and listed in Table 3.2. Samples located along profiles AA' and BB' in the hanging wall of the Aleutian trench and furthest from the deformation front have relatively high ages that range from 4.9 to 39.6 Ma. Samples located along profiles CC' and DD' in the hanging wall of the Yakutat terrane and within the deformation zone have lower ages that range from 1.0 to 18.3 Ma. The majority of samples located outside of the collision zone along AA', BB', and inland portions of CC' are older than the initial uplift age of the coastal mountains (5-6.7 Ma) (Lagoe et al., 1993). The youngest ages (1.0 to 5.8 Ma) are clustered in the southeastern portion of the field area, close to the syntaxial bend along CC' and DD'.

A marked decrease in age extending from the northern flanks of the range to the coast is exhibited (Figures 3.4-3.6). Ages along BB' decrease from a maximum of 36.5 Ma for an inland sample located southeast of the Copper River/Chitina River junction to 4.9 and 5.5 Ma samples located near the coast on either side of the Copper River, crossing both the Border Ranges fault system and the Contact fault system (Figures 3.4 and 3.5; Figure 2.1). Ages along CC' decrease from an 18.3 Ma inland sample located in the hanging wall of the active Chugach-St. Elias fault to a 1.4 Ma coastal sample located in the highly dissected fold-and-thrust belt in the footwall of the Yakutat terrane, crossing the Contact fault system north of the Chugach-St. Elias fault. Along profiles BB', CC', and DD', age is well correlated with distance from the coast and fits with previous AFT results where available (Figures 3.6 and 3.7). AFT ages in the Alaska panhandle decrease across strike from 4.4-4.5 Ma inland to 1.7-3.5 Ma closer to the coast (Figure 3.4) (O'Sullivan et al., 1997). Samples along the Alsek River to the southeast also decrease across strike from 2.5 Ma inland to 1.3 Ma along the coast, crossing the Fairweather fault.

Two age-elevation profiles can be plotted from these data (Figure 3.8). Sample suites suitable for age-elevation plotting (i.e. minimum horizontal separation, large relief in section) are rare in these data, given the logistical problems of sampling by helicopter on very steep terrain. Samples 02CH1, 2, and 4 along BB' from the hanging wall of the Aleutian trench define a 0.0063 Ma/m gradient over a 570 m increase in elevation (Figure 3.8). A second group, samples 99CH2, 01CH47, and 01CH48 along CC' in the hanging wall of the Chugach-St. Elias fault, shows a 0.0067 Ma/m gradient over a 1166 m gain in elevation (Figure 3.8). If these gradients

are inverted to reflect exhumation, rates are 0.16 mm/yr for BB' and 0.15 mm/yr for CC'. Exhumation rates are comparable between both profiles, but ages along BB' are from the Eocene (?) and ages along CC' are from the Miocene. Since these inland samples are old, the onset of collision by the Yakutat terrane is not constrained by these vertical profiles.

Over a quarter of the samples have errors higher than 10% typically assumed for the AHE technique (Table 3.2). The influence of poor-quality grains on sample ages is illustrated by large error bars in Figure 3.6. Samples 01CH4, 8, and 10 along AA' have the highest error bars for all of the samples, which likely reflect mineral inclusions not detected in the poor-quality apatite grains. 01CH10 stands out as an anomaly because it doesn't follow a southward decrease in age like samples 01CH4 and 8, despite being only ~50 km from shore. Sample 02CH3 along BB' has large error bars due to low concentrations of U and Th. The three other samples (02CH1, 2, and 4) collected at higher elevations along the vertical profile had acceptable concentrations of U and Th, so it is unclear why concentrations are so low for this sample. Two late Tertiary sandstone samples (01CH34 and 41) located in a coastal area close to the deformation front along CC' and DD' have ages that are as high as 16 Ma, but are believed to have not been heated above closure temperature since deposition (i.e. not reset) based on poor age reproducibility and young depositional age. The youngest sample of the suite (01CH43) along DD' has an error of 50%, but the variation in age does not affect the southward trend.

Figure Captions

Table 3.2 AHE ages for the Chugach-St. Elias Mountains.

Figure 3.4 Map of AHE ages and AFT ages previously measured by Long (1992), O'Sullivan and Currie (1996), and O'Sullivan et al. (1997). Elevation of samples can be seen along the four profiles in Figure 3.5. Sample ages in the hanging wall of the Aleutian trench along profiles AA' and BB' are significantly higher than those in the footwall of the Yakutat terrane along CC' and DD'. A decrease in age occurs towards the coast along BB' and CC', but is less apparent on AA' and DD'. NR = not reset.

Figure 3.5 Ages plotted on elevation-distance profiles for the four profiles shown in Figure 3.4. Sample locations were projected onto the nearest profile. Elevations along profiles are from 60 m grid digital elevation models (DEMs) and 1:63360 topographic maps.

Figure 3.6 Age versus distance from coast for all dated samples along the four profiles. Ages decrease towards the coast. 01CH4, 8, and 10 from profile AA' have large error bars likely due to poor-quality apatite grains and 02CH3 has large error bars from low U-Th concentrations. Samples 01CH34 and 41 were not reset (NR), but the maximum age was plotted. One AFT sample close to the Chugach-St. Elias fault (O'Sullivan et al., 1997) and two at low elevations of Mt. Logan (O'Sullivan and Currie, 1996) are also plotted.

Figure 3.7 High R^2 values for BB' and CC' indicate that ages are well correlated with distance from the coast (R^2 of 1 reflects 100% correlation between plotted points and the trendline). Profile BB' is outside of the collision zone, while CC' extends through the collision zone, crossing the Chugach-St. Elias fault ~50 km from shore.

Figure 3.8 Age-elevation plots for vertical sample suites from northern BB' and CC'. Similar age-elevation gradients from both plots suggest that each area experienced slow exhumation in the early- to mid-Tertiary, prior to the onset of Yakutat collision.

Table 3.2: AHE data for the Chugach-St. Elias Mountains (27 samples).

Sample	Elevation m	Latitude, Longitude	Rock Type	Mass, mg	mwar, µm	He, pmol	U, ppm	Th, ppm	# grains	Measure cycle	FT	Corr. Age, Ma	Average Age, Ma	T _c , °C _b
99CH1-1A	46	60.4779°, 145.3375°	gr.	0.0173	35.1	0.0121	30.7	8.5	19	Summer '03	0.63	6.5	6.3±0.6	61
99CH1-1B				0.0252	38.1	0.0168	28.2	9.3	19	Summer '03	0.68	6.2		
99CH2-1	754	60.7203°, 142.5435°	gn.	0.0366	55.8	0.0455	38.9	4.3	15	Winter '02	0.77	7.8	8.2±0.8	61
99CH2-2				0.0202	42.0	0.0307	50.5	2.8	23	Winter '02	0.67	8.5		
01CH4-1	1417	61.5346°, 145.3263°	m-gr.	0.0063	53.2	0.0071	3.7	30.0	2	Winter '02	0.76	25.8**	34.1±10.2	50
01CH4-2				0.0099	30.9	0.0079	4.0	9.3	19	Winter '02	0.58	42.4**		
01CH8-1	1174	61.2979°, 145.3206°	m-gr.	0.0067	28.5	0.0136	19.6	29.6	17	Winter '02	0.56	25.8**	25.8±7.7	47
01CH10-1	671	61.0712°, 145.9888°	sch.	0.0048	25.7	0.0050	11.3	16.7	18	Winter '02	0.51	34.2**	39.6±11.9	46
01CH10-3				0.0041	30.9	0.0132	19.8	27.8	15	Spring '02	0.52	44.9**		
01CH22-1	1532	60.9104°, 144.3150°	sch.	0.0077	33.1	0.0194	33.3	27.8	11	Spring '02	0.64	20.1	20.1±2.0	50
01CH22-3				0.0035	25.7	0.0072	38.6	17.3	12	Spring '02	0.52	17.7*		
01CH26-1	884	60.4990°, 144.4772°	gran.	0.0086	34.7	0.0036	27.9	15.5	12	Winter '02	0.64	3.9**	4.9±1.5	60
01CH26-2				0.0041	30.3	0.0035	40.4	30.5	10	Winter '02	0.58	5.8**		
01CH28-1	564	60.4926°, 145.2510°	gran.	0.0213	34.6	0.0114	27.1	6.6	24	Winter '02	0.63	5.7	5.5±0.6	61
01CH28-2				0.0284	45.8	0.0146	24.7	7.7	17	Winter '02	0.72	5.2		
01CH29-1	1082	60.2926°, 142.3558°	ss.	0.0173	34.8	0.0070	26.0	22.5	21	Spring '03	0.63	3.9	3.9±0.4	63
01CH34-2	579	60.2134°, 142.6270°	ss.	0.0105	31.3	0.0020	12.0	13.7	15	Winter '02	0.61	3.9*	NR	
01CH34-3				0.0129	34.9	0.0137	20.7	20.5	17	Spring '02	0.64	12.4		
01CH38-1	640	60.3194°, 143.1168°	grwk.	0.0282	45.2	0.0050	28.9	31.5	19	Spring '03	0.71	1.3	1.4±0.2	75
01CH38-2				0.0291	43.3	0.0055	26.4	30.1	20	Spring '03	0.72	1.5		
01CH39-1	297	60.2625°, 143.3121°	grwk.	0.0183	33.6	0.0031	18.3	23.4	26	Spring '03	0.61	2.3	2.2±0.2	66
01CH39-2				0.0178	33.3	0.0045	30.5	38.8	27	Spring '03	0.62	2.0		
01CH41-1	274	60.0592°, 141.9400°	grwk.	0.0096	28.4	0.0191	34.0	31.0	24	Fall '02	0.56	16.3	NR	
01CH43-1	279	60.1809°, 141.1756	grwk.	0.0164	38.3	0.0017	28.2	31.3	20	Winter '02	0.64	0.9**	1.0±0.5	76
01CH43-3				0.0049	26.5	0.0004	36.4	36.0	13	Spring '02	0.54	0.6**		
01CH43-4				0.0130	29.5	0.0013	19.3	24.4	29	Fall '02	0.58	1.4**		
01CH45-1	1783	60.6572°, 142.4146°	gran.	0.0435	72.9	0.0848	52.6	1.6	18	Spring '02	0.78	9.0	9.7±1.0	65
01CH45-2				0.0227	49.9	0.0368	41.9	1.6	15	Spring '02	0.75	9.8		
01CH45-3				0.0444	105	0.1529	71.8	1.5	2	Spring '02	0.89	10.3		

Table 3.2: continued.

Sample	Elevation m	Latitude, Longitude	Rock Type	Mass, mg	mwar, µm	He, pmol	U, ppm	Th, ppm	# grains	Measure cycle	F _T	Corr. Age, Ma	Average Age, Ma	T _c , °C _b
01CH47-1	1494	60.7672°, 142.6065°	sch.	0.0103	33.3	0.0213	45.3	3.6	21	Fall '02	0.60	14.3	13.3±1.3	54
01CH47-2				0.0222	44.7	0.0396	39.1	3.2	21	Spring '03	0.70	12.3		
01CH48-3	1920	60.7911°, 142.6368°	sch.	0.0073	30.9	0.0053	11.0	13.0	15	Spring '02	0.61	16.0	16.0±1.6	49
01CH48-4				0.0066	33.8	0.0029	8.9	16.1	22	Fall '02	0.56	11.9*		
01CH49-1	2012	60.6793°, 142.5340°	gn.	0.0111	41.1	0.0105	21.0	0.3	20	Fall '02	0.62	13.8	13.0±1.3	55
01CH49-2				0.0182	41.6	0.0212	26.7	0.6	17	Spring '03	0.69	12.1		
01CH56-1	1135	60.2482°, 141.1171°	grwk.	0.0140	37.9	0.0038	13.6	14.5	17	Summer '03	0.67	4.6	5.8±0.6	62
01CH56-2				0.0118	35.2	0.0049	13.6	17.3	17	Summer '03	0.64	7.0		
02CH1-1	1829	61.3408°, 144.2049°	diorite	0.0198	40.1	0.0181	5.9	9.9	20	Spring '03	0.67	31.5	28.7±2.9	51
02CH1-2				0.0202	39.3	0.0200	8.2	11.8	20	Spring '03	0.66	25.8		
02CH2-1	1524	61.3425°, 144.1896°	diorite	0.0134	33.3	0.0161	9.1	13.9	19	Spring '03	0.63	29.4	29.8±3.0	50
02CH2-2				0.0152	36.1	0.0168	8.0	12.5	19	Spring '03	0.63	30.1		
02CH3-1	1074	61.3231°, 144.1405°	phyl.	0.0183	44.2	0.0049	1.6	1.7	17	Spring '03	0.69	36.5 ^a	36.5±7.2	52
02CH4-1	1259	61.3344°, 144.1521°	diorite	0.0152	35.0	0.0202	9.4	19.2	19	Spring '03	0.65	28.0	27.9±2.8	50
02CH4-2				0.0139	36.2	0.0180	9.5	18.2	17	Spring '03	0.65	27.7		
02CH19-1	1402	60.9221°, 142.4012°	diorite	0.0231	44.4	0.0492	24.7	27.4	16	Summer '03	0.71	18.4	18.3±1.8	53
02CH19-2				0.0160	37.7	0.0385	31.9	30.7	17	Summer '03	0.64	18.3		
02CH28-1	1625	60.2573°, 141.1584°	grwk.	0.0122	35.6	0.0057	35.6	32.6	19	Summer '03	0.62	3.3	4.8±1.5	61
02CH28-2				0.0121	37.2	0.0089	25.5	38.4	16	Summer '03	0.65	6.3		
02CH31-1	1387	60.2855°, 141.4542°	grwk.	0.0225	44.4	0.0029	20.6	28.5	19	Summer '03	0.70	1.2	1.2±0.1	70
02CH31-2				0.0184	38.1	0.0023	23.0	32.0	22	Summer '03	0.66	1.3		
02CH32-1	1478	60.3435°, 141.7640°	ss.	0.0181	40.2	0.0024	20.1	26.0	20	Summer '03	0.66	1.4	1.5±0.2	67
02CH32-2				0.0159	35.2	0.0031	27.0	39.0	20	Summer '03	0.63	1.7		

mwar = mass-weighted average radius; T_c = assumed closure temperature

2σ uncertainties = ±10%.

*High error due to low gas relative to line blank (~30%); age not used for average, but reported to indicate consistency in result. Note that analyses from Spring and Summer 2003 were made with higher helium sensitivity due to improvements in technique.

**High error due to low gas relative to line blank, but used to compute average due to no better data (30% error).

^a20% error due to low gas associated with low U/Th.

^bClosure temperature (T_c) is based on average grainsize (mwar) (38) and the cooling rate for the average age (iterative solution).

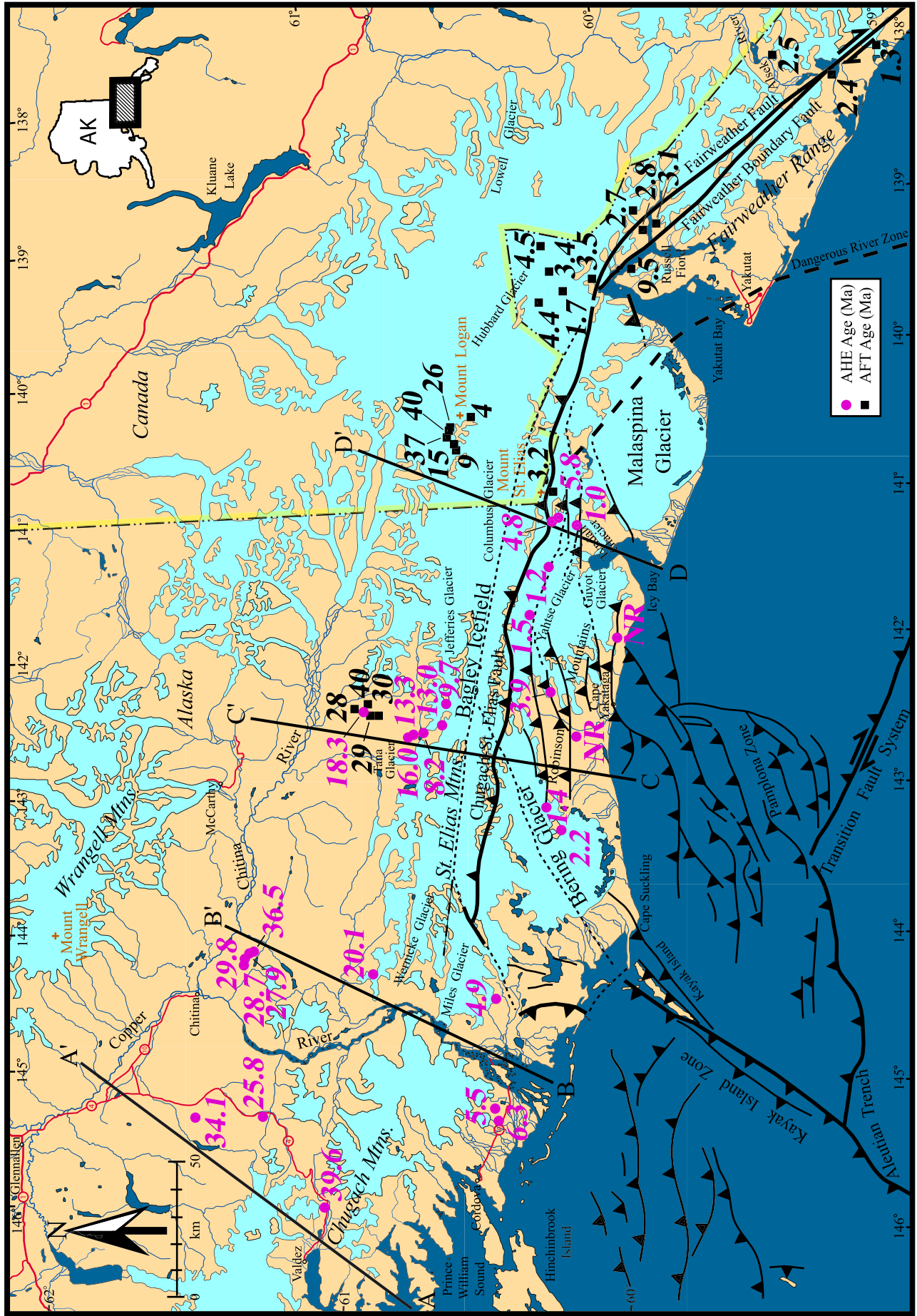


Figure 3.4

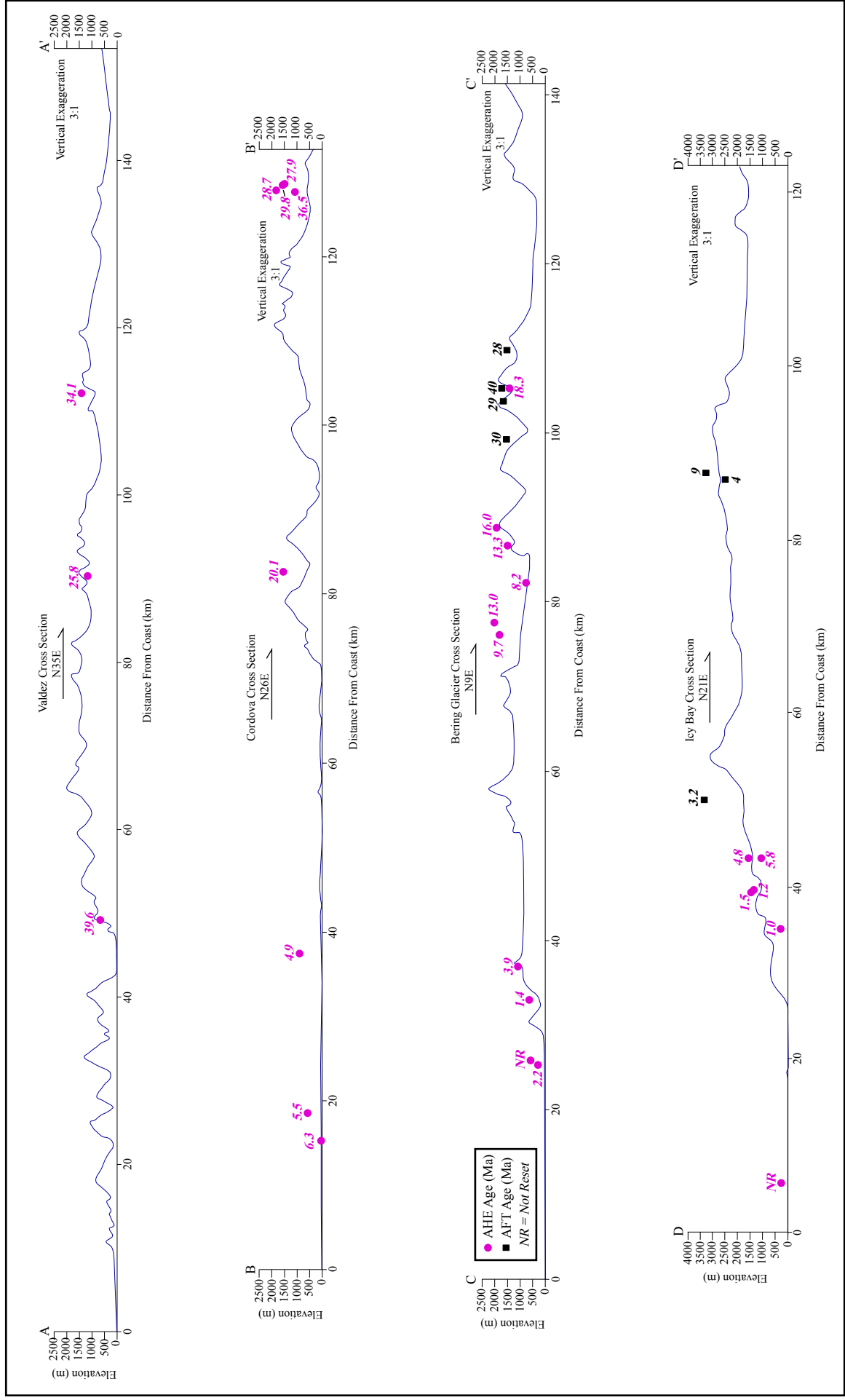


Figure 3.5

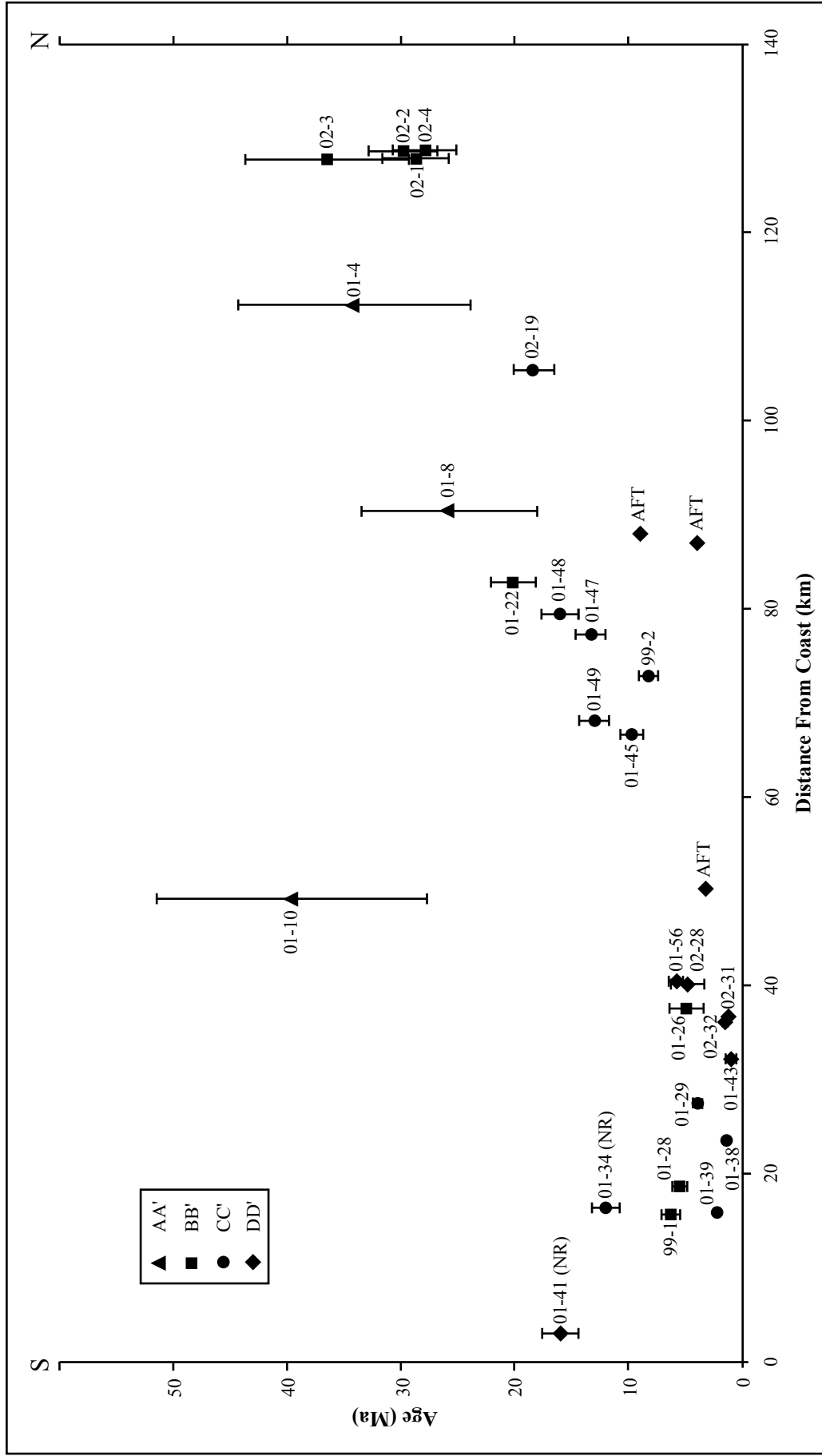


Figure 3.6

Figure 3.7

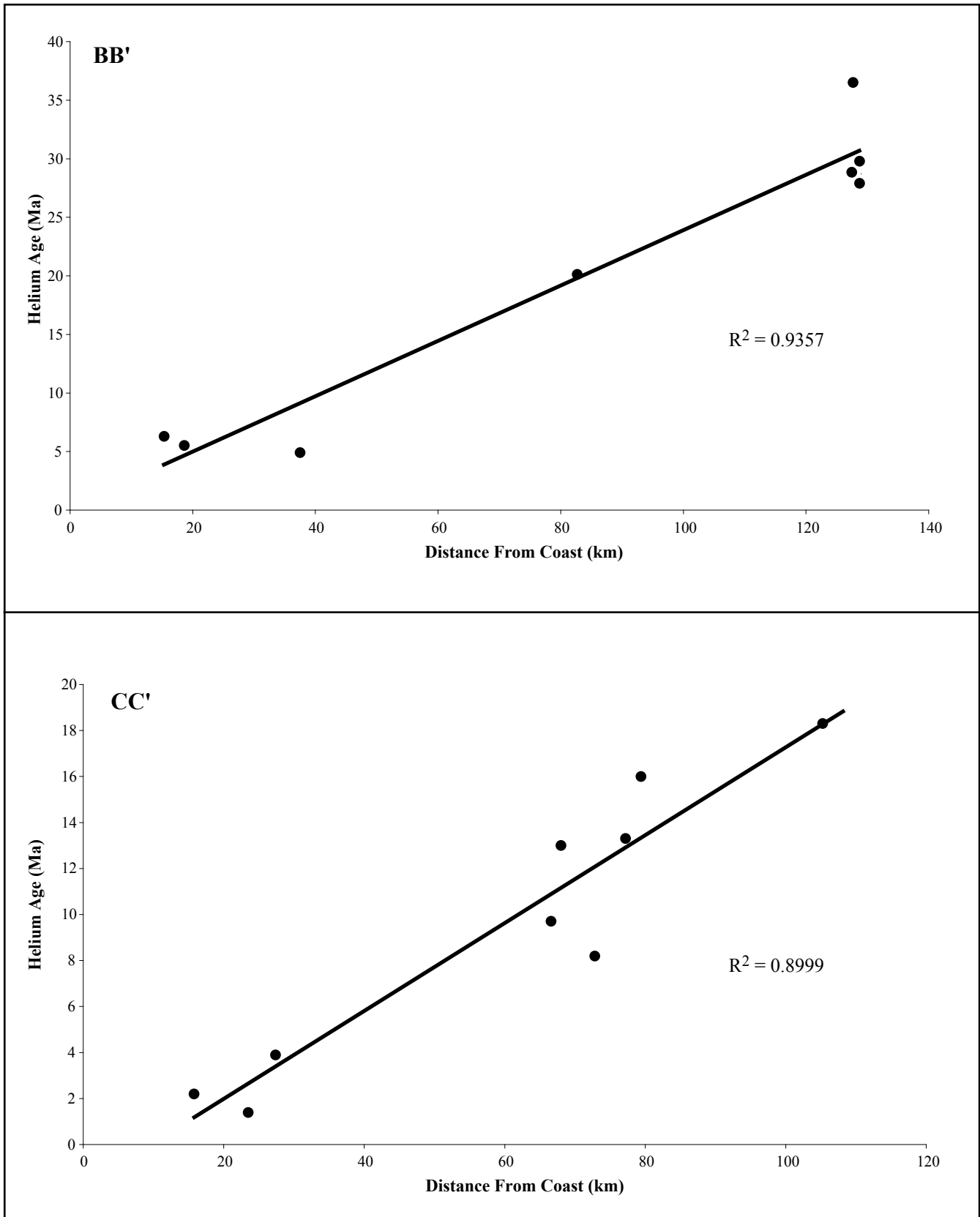
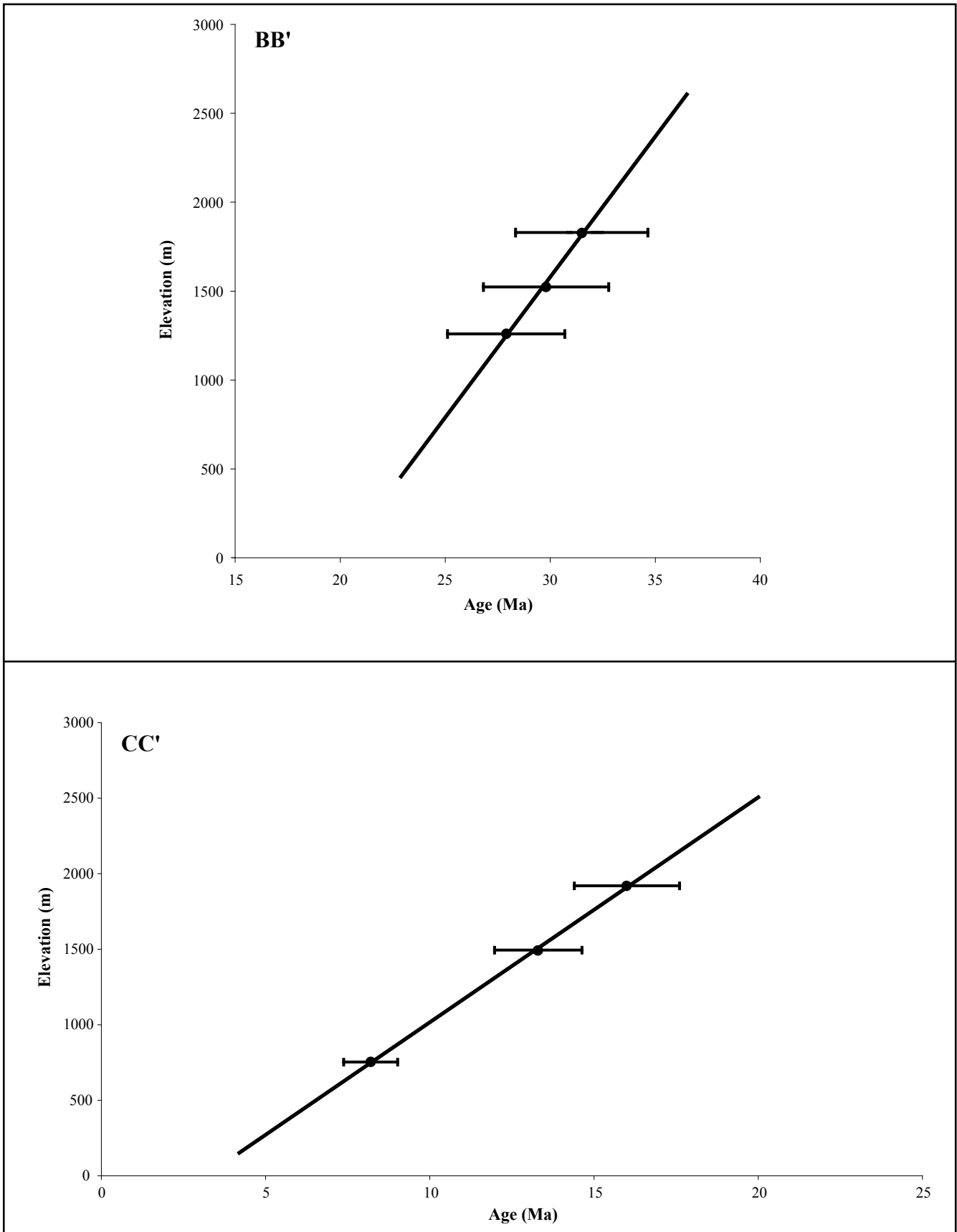


Figure 3.8



CHAPTER 4: INTERPRETATIONS AND DISCUSSION

4.1 Inferring Exhumation

AHE ages are used to determine exhumation rates, based on the closure temperature (T_c) of each sample and an assumed geothermal gradient. The T_c was assigned iteratively using the mass-weighted-average radius of each sample and the best-fit cooling rate from the average age (Table 3.2) (Farley, 2000). The geothermal gradient is assumed to be 30°C/km for southern Alaska. A shallow gradient of 20°C/km is established from petroleum wells for the Gulf of Alaska, whereas ~36°C/km was inferred from the AFT partial annealing zone at Mt. Logan (O'Sullivan and Currie, 1996; O'Sullivan et al., 1997). Given uncertainty in geothermal gradient, absolute exhumation rates could be off by up to 20-30%, but relative differences should be accurate. As shown below, these uncertainties are smaller than significant differences in exhumation rate and short-term rate. The inferred T_c depth is used with each AHE age to calculate an exhumation rate, assuming a vertical trajectory from the helium partial retention zone to the earth's surface. Exhumation rates for each sample are listed in Table 4.1.

Exhumation rates increase sharply across the strike of the range towards the coast and weakly along-strike towards the syntaxial bend in the east (Figures 4.1 and 4.2). The sharpest increase in exhumation towards the coast is along CC' (~18-fold), although this is also clear on BB' and DD'. The increase is more abrupt on DD'. A distinct exhumation pattern is not recognized along profile AA'.

Age-elevation relationships offer additional clues for exhumation and uplift history. An age-elevation relationship for samples from northern BB' is ~0.16 mm/yr (Figure 4.3). An age elevation gradient for northern CC' is ~0.15 mm/yr. These gradients are comparable, although the periods they represent are different (late-Oligocene to early-Miocene for BB', mid- to late-Miocene for CC'). This difference reflects a variation in the total amount of rock eroded from the surface (Figure 4.3). Samples from both profiles moved through the HePRZ at similar rates, but rocks along CC' exhumed at faster rates through depths above the HePRZ. Projection of the age-elevation trendline from BB' to CC' suggests ~2.5 km more exhumation along CC'. A similar comparison can be made for AFT ages from CC' and DD'. These ages are comparable (~28-40 Ma) but differ in elevation by ~4 km (Figure 4.4) (Long, 1992; O'Sullivan and Currie, 1996). This indicates greater rock uplift or sustained higher elevations at Mt. Logan since the early-

Oligocene. These comparisons are consistent with an increase in exhumation from west to east calculated above.

4.2 Comparison of Exhumation and Tectonic Features

The steady increase in exhumation from west to east (Figure 4.1) towards the collision zone may reflect tectonics. Rates are much higher in the collision zone (CC', DD') than above the subduction zone in the Chugach Range (AA', BB'). This is consistent with tectonics playing a primary role in the basic rock uplift and denudation pattern. The across-strike increase in exhumation does not correlate with active faults or major terrane boundaries (Figures 2.1, 4.2, and 4.5). Profile BB' crosses the Border Ranges fault, Contact fault system, and subsidiary post accretion strike-slip faults in the south, but exhumation increases steadily from the Chitina River to the mouth of the Copper River (Plafker, 1987; Plafker et al., 1994b). In addition to crossing the Border Ranges and Contact faults, profile CC' crosses the highly-active Chugach-St. Elias fault system and the northern Pamplona fold and thrust belt. Fault activity thus increases southward from the inland terrane boundary faults to the deformation front of the Yakutat terrane (Plafker, 1987; Plafker, 1994b).

There is a basic correlation between deformation intensity and denudation. The Yakutat deformation front has the highest exhumation rates in the range. However, one sample close to the Chugach-St. Elias fault in the footwall yields a lower exhumation rate than others in the Yakutat terrane, but further from the fault, suggesting deformation in this zone is not the exclusive control on exhumation. Many aspects of the tectonics do not seem to affect denudation. For example, exposure of deep rocks (metamorphosed flysch) in the hanging wall of the Chugach-St. Elias fault contradicts the steady southward increase in exhumation. Also, the southward increase in exhumation contrasts with a southward flattening of structural dip (Figure 4.6) (Plafker, 1987; Plafker et al., 1994b). This implies that either fault slip rate increases to the south or that structural orientation does not affect rock uplift here. Profile DD' crosses the same structures as CC' and shows a similar southward increase in exhumation. Like on CC', exhumation is fastest in the footwall of the CSEF, and does not relate as expected to the northward increase in fault dip. However, there is also local variation in this region, such as slower rates for 01CH56 and 02CH28, which are close to the youngest age. Inferring age-elevation relationships from localized structures and stratigraphy proves to be difficult in an area

where constraints on fault orientations and stratigraphic burial depths are not well known. Thus, the influence of tectonic structure on exhumation pattern is not entirely clear in the CSEM.

AFT data in the eastern portion of the St. Elias Mountains also demonstrates a mismatch between exhumation and structural pattern (O'Sullivan et al., 1997). Exhumation rates increase from the syntaxial bend to the southeast along the Yakutat plate southwest of the Fairweather fault. Exhumation also increases across and to the north of the syntaxial bend along the Fairweather fault. This is surprising, given that deformation intensity should peak at the syntaxial bend. This may be due to transpression on the Fairweather fault as suggested by oblique displacement from the 1958 earthquake and field evidence (Plafker, 1987; Plafker et al., 1994b). However, GPS data from Yakutat and Cape Yakataga suggest that the Pacific plate is moving parallel to the fault (Sauber et al., 1997; Fletcher and Freymueller, 1999). One difference between DD' and other profiles is also indicated by AFT. Exhumation rates at Mt. Logan are similar to those closer to shore and this shows that there is no decrease northward (O'Sullivan et al., 1997). This indicates no big changes across faults and terrane boundaries, but also less of an effect of climate.

4.3 Comparison of Exhumation and Glacial Climate

Patterns of exhumation strongly correlate with local climate (precipitation, ELA) (Figure 4.7). Feedbacks between topography, precipitation, ELA, and erosion may be responsible for these relationships. Mean annual precipitation, dominated by storms sourced from the Gulf of Alaska, decreases across strike from 2-3 m/yr along the windward side of the range to less than 0.5 m/yr on the leeward side (Jaeger et al., 1998; Meigs and Sauber, 2000). As a result, modern ELA rises from ~600 m near the coast to ~2200 m inland in the center of the range. ELA increases slightly along strike from west to east, partly due to precipitation and partly from the effect of topography on ELA itself (Meigs and Sauber, 2000). The distribution of glaciers also increases southwards and eastwards (Figures 2.5 and 2.7). These trends correlate with the increase in exhumation southwards and eastwards. Greater precipitation, lower ELA, and more glaciers may translate to faster erosion and greater long-term exhumation. Coastal samples along AA' and BB' are outside of the immediate collision zone and cross two major tectonic boundaries that exhibit only minor activity, yet exhumation is seven times greater along the coast than for inland areas. The same is true for CC' and DD', although rates are generally higher. The fastest local exhumation rates occur near the largest outlet glaciers (Bering, Yahtse, and Tyndall

glaciers), while slow rates occur in between. This might indicate that erosion is greater along larger glaciers. Heavy glacial erosion on the windward flank of the Fairweather range may also explain the unexpected rapid exhumation indicated by AFT (O'Sullivan et al., 1997). Thus, the across-strike increase in exhumation and its lack of correlation to major tectonic boundaries suggests that glaciers are controlling landscape development.

Topography of the CSEM illustrates the impact of glaciers on the landscape (Figure 4.8). A comparison of slope and elevation shows that there is a strong relationship to ELA (Meigs and Sauber, 2000). Slopes are low at elevations from ~2000 m to sea level corresponding to the across-strike range in ELA. Above ELA, slopes increase dramatically. However, very little land area extends above ELA (only local ridges), whereas the majority of the landscape is clustered near ELA. This relationship between topography and ELA suggests glaciers have a primary role in shaping and limiting elevations.

4.4 Comparison of Long-Term Exhumation Rates and Short-Term Sediment Yield

Long-term exhumation rates inferred by thermochronometry are considerably lower than short-term effective erosion rates inferred from sediment deposition. Maximum exhumation rates inferred from ages at the 10^6 -year scale for the entire range are 0.5-1 mm/yr. Effective erosion rates at Holocene time scales on the continental shelf are up to 5 mm/yr (Jaeger et al., 2002; Sheaf et al., 2003). Rates inferred from 100-year sediment accumulation rates in fjords can be 10s of mm/yr (Hallet et al., 1996). The variation in erosion rates reflects how time and location can influence the manifestation of glacial processes.

Effective erosion rates inferred from sedimentation in fjords over 100-year time scales (Hallet et al., 1996) can be more than 20 times greater than rates inferred from AHE ages. The short-term rates may reflect transients that do not represent exhumation averaged over many glacial cycles. These rates have also recently been attributed in part to rapid glacial retreat from the Little Ice Age period (Koppes and Hallet, 2002). The method of inferring erosion rates from fjord deposition is subject to inaccuracy due to sediment storage and recycling and interpretation of fjord geometry. Short-term rates have been used to characterize the power of glacial erosion, but may over-predict what is feasible for long-term exhumation. The impact of glacial erosion on orogens inferred from fjord deposits may thus be exaggerated.

Effective erosion rates over Holocene time scales in the Gulf of Alaska are slightly higher than exhumation rates inferred from AHE ages. Sheaf et al. (2003) estimate average Holocene

rates of 5.1 mm/yr, whereas Jaeger et al. (2002) report rates of 1.5, 3.5, and 5.0 mm/yr for the Copper River, Bering glacier, and Malaspina glacier, respectively. The assumption that the first seismic reflector observed at depth is the Holocene boundary and that stacking velocities are representative of marine rocks at depth may be responsible for these variations in Holocene rates. These are all higher than average rates of long-term exhumation. Short-term rates inferred for the entire Gulf area (100-year time scales) are actually a bit slower. Effective erosion rates calculated from 100-year core samples from the shelf are a minimum of ~1-2 mm/yr, while rates for the Copper River, Bering glacier, and Malaspina glacier are 1.0, 2.5, and 3.0 mm/yr, respectively (Jaeger et al., 2002). This similarity between inferred average rates based on shelf sediments from Holocene to 100-year time scales suggests the 100-year extreme rates in fjords do not affect the entire sedimentation system. Glacial erosion may thus be more temporally uniform when considered at the orogen scale. However, long-term (10^6 -year) exhumation rates are still slower than estimates from 10^4 or 10^2 -year rates.

4.5 Conclusions

The average exhumation rate inferred from AHE ages is estimated to be 0.5-1 mm/yr for the CSEM, with localized coastal rates reaching a maximum of 2.5 mm/yr. Along and across-strike increases in rates towards the deformation front clearly demonstrate that the collision zone is the locus of maximum exhumation in the CSEM. However, exhumation is highest along the coast, contrary to an expected maximum in the core of the range where fault dip angles are higher and deep crustal rocks are exposed. The correlation of relatively high exhumation rates, large piedmont glaciers, and low ELA and topography along the coast supports glacial erosion as a primary force in landscape development. Also, higher rates proximal to the Bering, Yahtse, and Tyndall glaciers suggest that large glaciers might act as “glacial aneurysms”, where erosion is more efficient along established glaciers. However, coastal exhumation rates are still considerably lower than short-term rates inferred from sedimentary yields, suggesting that widely-accepted effective erosion rates over short time scales are not representative of long-term rates. Although these rates are low, the pattern of across-strike exhumation coupled with the distribution of glaciers supports the glacial buzzsaw hypothesis.

Figure Captions

Table 4.1 Exhumation rates were determined by using the T_c depth and the AHE age for each sample. ^aDepth is based on T_c for each sample and an assumed geothermal gradient of 30°C/km. NR = not reset.

Figure 4.1 Distribution of exhumation rates inferred from AHE and AFT ages in mm/yr. AHE rates were determined by using the age, T_c depth, and a geothermal gradient of 30°C/km. AFT rates were determined by using the age, an assumed closure temperature of 110°C, and a geothermal gradient of 30°C/km. Exhumation rates for AFT samples along DD' and in the eastern St. Elias Mountains were calculated from data by O'Sullivan and Currie (1996) and O'Sullivan et al. (1997). Rates for AFT samples along CC' were calculated from data by Long (1992).

Figure 4.2 Contoured exhumation rates for AHE and AFT ages in the CSEM. Colors indicate relative scale of exhumation rate: green lines = 0.08 to 0.3 mm/yr; yellow lines = 0.5 to 0.8 mm/yr; red lines = 1.0 to 2.0 mm/yr. Arrows show direction of increasing exhumation. Length of arrows shows spatial extent of exhumation increase.

Figure 4.3 AHE age-elevation plot for BB' and CC'. Projection of BB' trendline to an age shared with CC' suggests that the younger ages of CC' represent ~2.5 km more exhumation than BB'.

Figure 4.4 AFT age-elevation plot for CC' and DD'. Vertical projection of CC' to DD' suggests that there has been ~4 km more exhumation (or higher sustained mean elevations) along DD' than CC'. AFT plot along CC' is based on data from Long (1992). AFT plot along DD' is based on data from O'Sullivan and Currie (1996).

Figure 4.5 Best-fit curve for plot of exhumation rate versus distance from coast for all AHE samples except for the two that were not reset. Exhumation steadily increases towards the coast with no apparent influence of tectonic features.

Figure 4.6 Schematic diagram comparing exhumation inferred from AHE ages and that expected from tectonics, based on fault orientations and exposure of deep metamorphic rocks in the core of the range.

Figure 4.7 A strong correlation exists between exhumation, ELA, and precipitation. Both exhumation and precipitation increase towards the coast while ELA decreases. ELA and precipitation data from Meigs and Sauber (2000).

Figure 4.8 Slope-elevation plot for the Chugach-St. Elias Mountains (CSEM). The black line is the 50th percentile of slopes located in the CSEM, and the gray lines are the 25th (below), and 75th (above) percentiles. Figure from Meigs and Sauber (2000).

Table 4.1

Sample	Profile	^aDepth of T_c (km)	Inferred Exhumation Rate (mm/yr)
99CH1	BB'	2.0	0.32
99CH2	CC'	2.0	0.24
01CH4	AA'	1.7	0.05
01CH8	AA'	1.6	0.06
01CH10	AA'	1.5	0.04
01CH22	BB'	1.7	0.09
01CH26	BB'	2.0	0.41
01CH28	BB'	2.0	0.36
01CH29	CC'	2.1	0.54
01CH34	CC'	NR	NR
01CH38	CC'	2.5	1.8
01CH39	CC'	2.2	1.0
01CH41	DD'	NR	NR
01CH43	DD'	2.5	2.5
01CH45	CC'	2.2	0.23
01CH47	CC'	1.8	0.14
01CH48	CC'	1.6	0.10
01CH49	CC'	1.8	0.14
01CH56	DD'	2.1	0.36
02CH1	BB'	1.7	0.06
02CH2	BB'	1.7	0.06
02CH3	BB'	1.7	0.05
02CH4	BB'	1.7	0.06
02CH19	CC'	1.8	0.10
02CH28	DD'	2.0	0.42
02CH31	DD'	2.3	1.9
02CH32	DD'	2.2	1.5

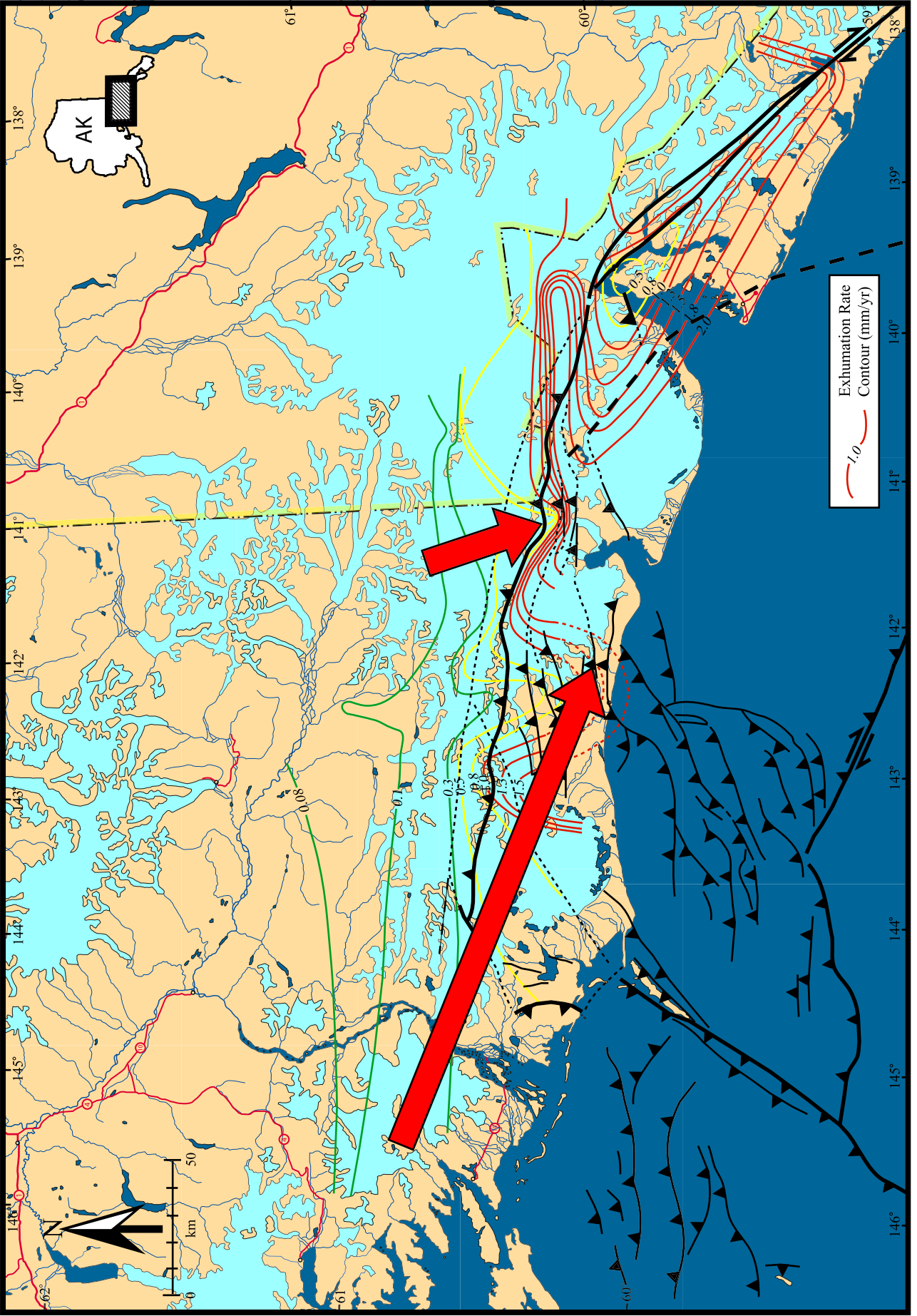


Figure 4.2

Figure 4.3

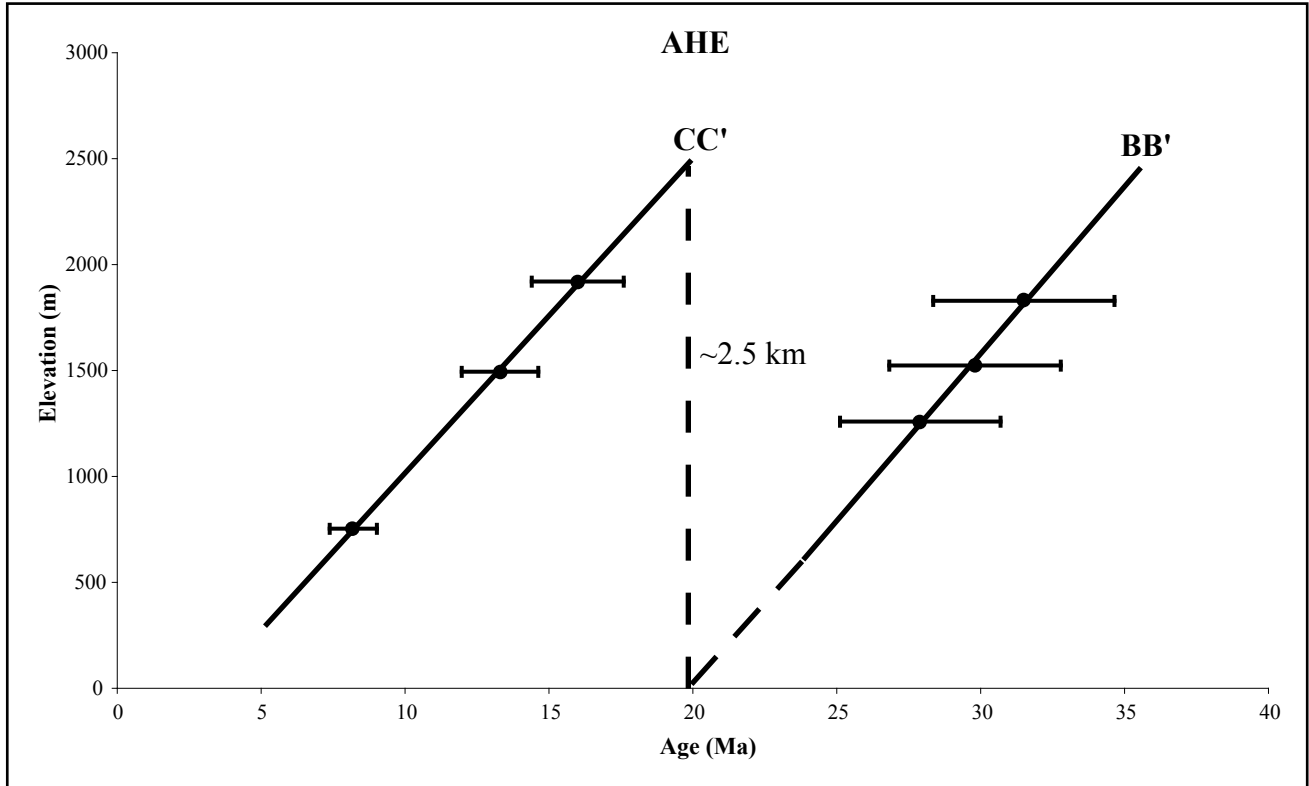


Figure 4.4

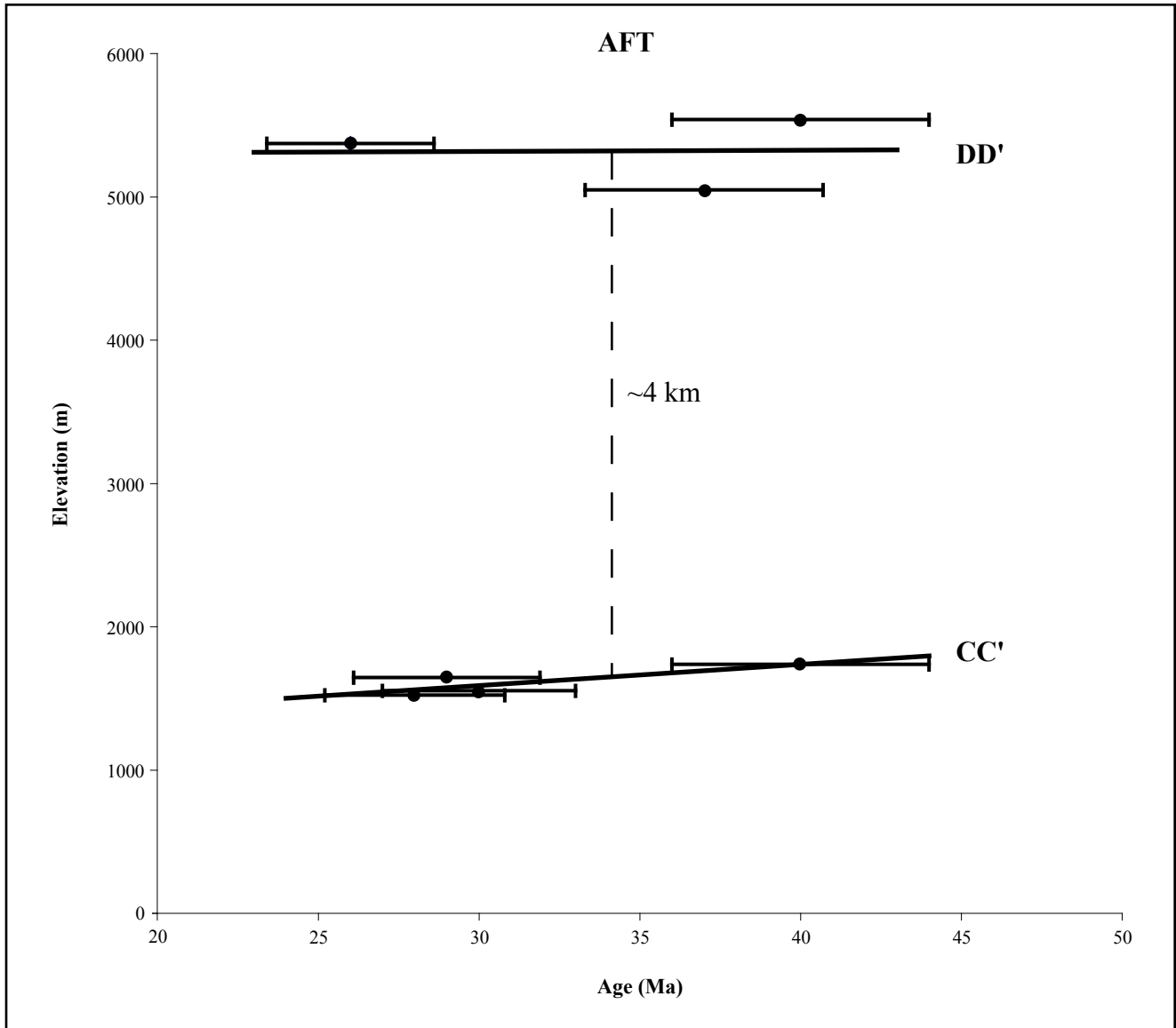


Figure 4.5

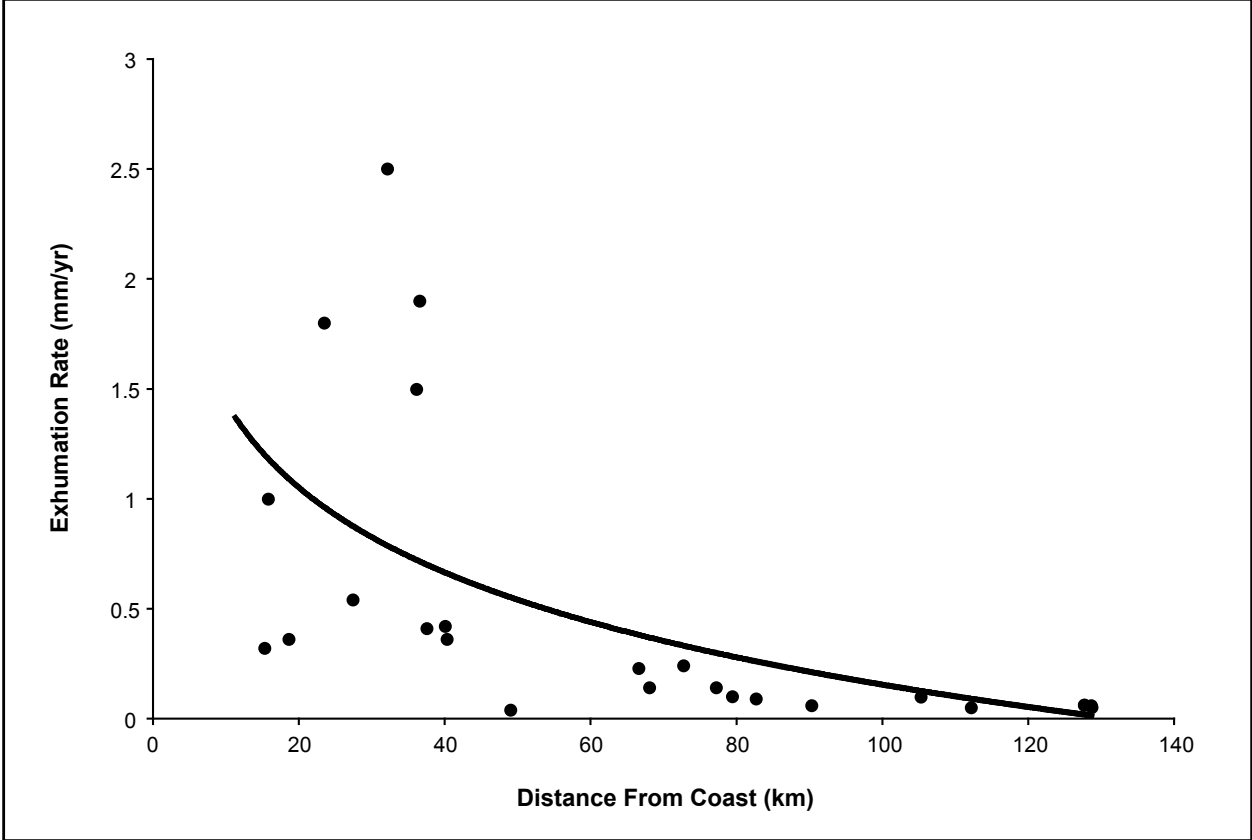
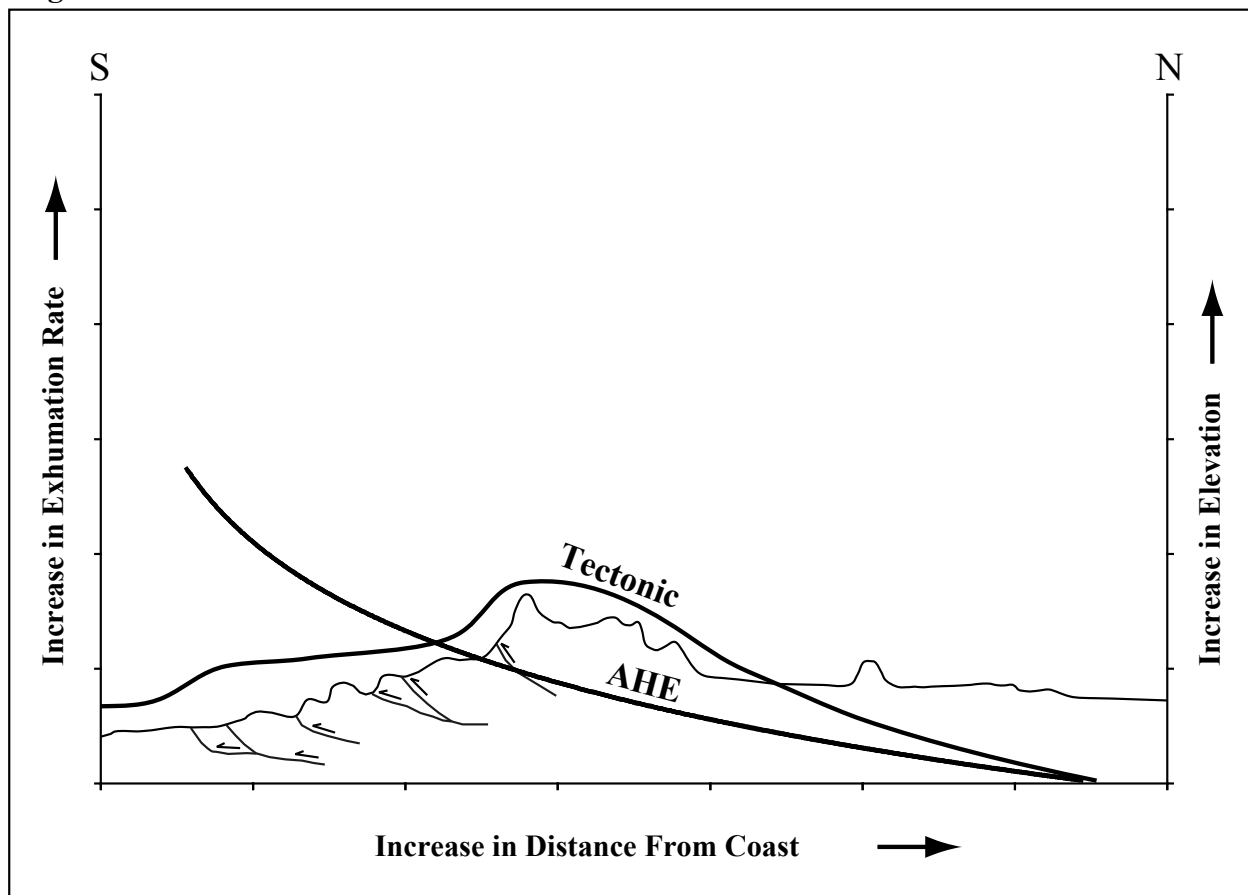


Figure 4.6



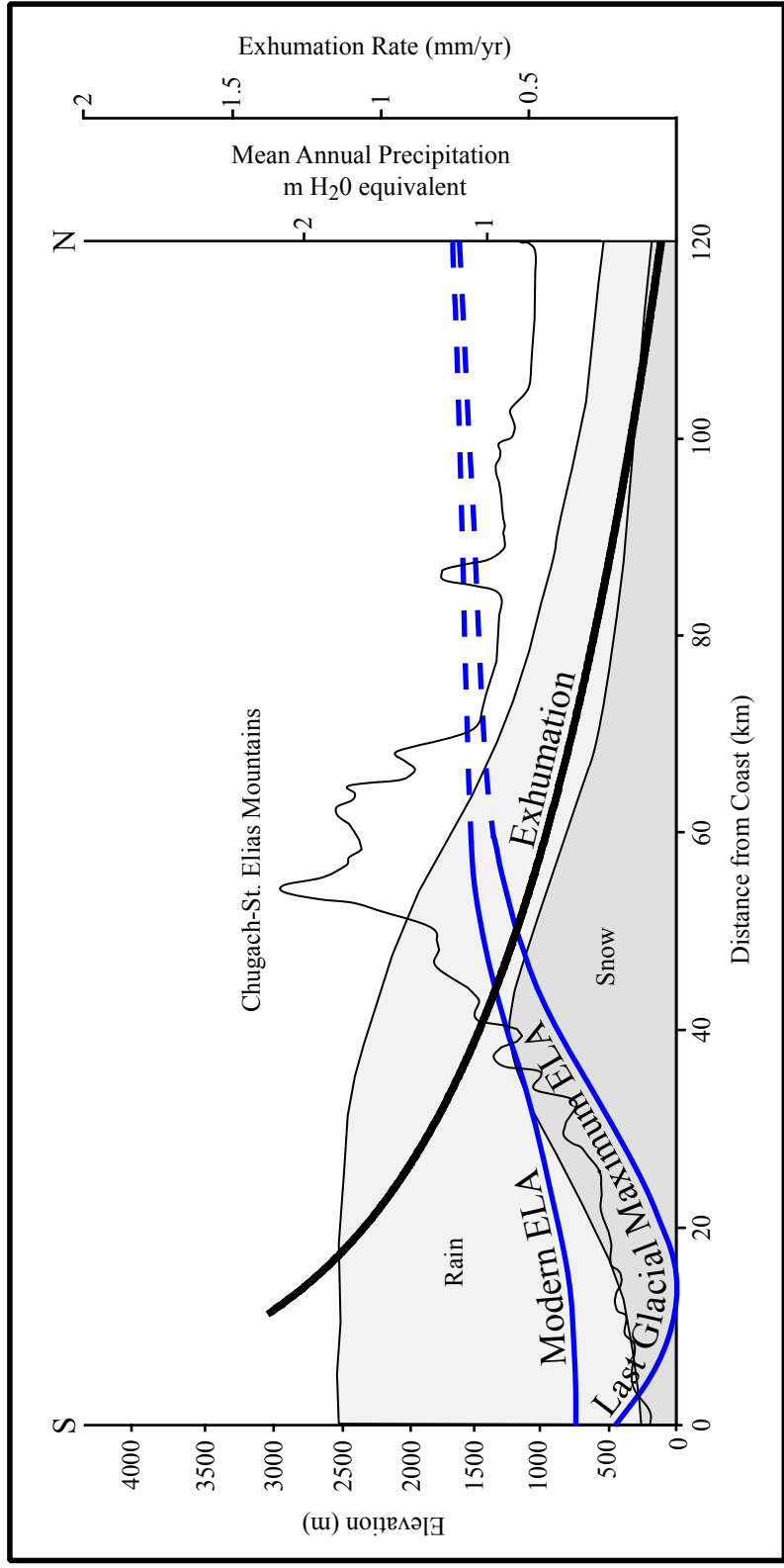
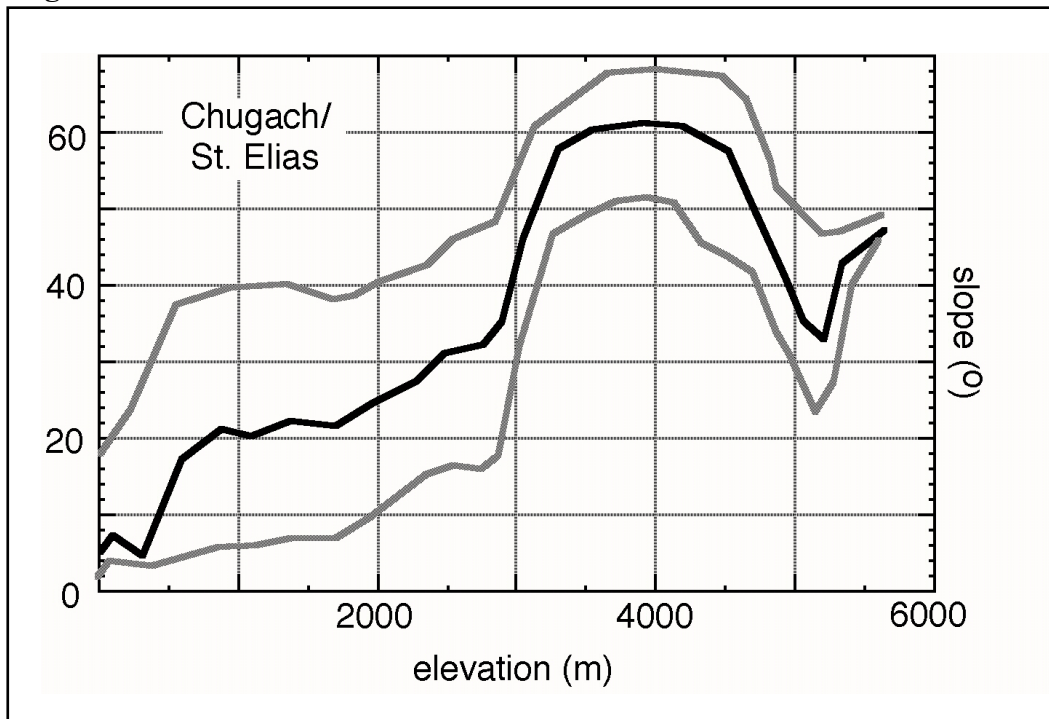


Figure 4.7

Figure 4.8



References Cited

- Andrews, J.T., 1972, Glacier power, mass balances, velocities, and erosion potential: *Zeitschrift für Geomorphologie*, v. 13, p. 1-17.
- Bird, P., 1996, Computer simulations of Alaskan neotectonics: *Tectonics*, v. 15, no. 2, p. 225-236.
- Brocklehurst, S.H. and Whipple, K.X., 2002, Glacial erosion and relief production in the Eastern Sierra Nevada, California: *Geomorphology*, v. 42, p. 1-24.
- Brozović, N., Burbank, D.W., and Meigs, A.J., 1997, Climatic limits on landscape development in the northwestern Himalaya: *Science*, v. 276, p. 571-574.
- Bruhn, R.L., Pavlis, T.L., Plafker, G., and Serpa, L., in press, Deformation during terrane accretion in the Saint Elias orogen, Alaska: *Geological Society American Bulletin*.
- Csejtey, B., Jr., Cox, D.P., Evarts, R.C., Stricker, G.D., and Foster, H.L., 1982, The Cenozoic Denali Fault System and the Cretaceous accretionary development of southern Alaska: *Journal of Geophysical Research*, v. 87, no. B5, p. 3741-3754.
- DeMets, C., Gordon, R.G., Argus, D.F., and Stein, S., 1990, Current plate motions: *Geophysical Journal International*, v. 101, no. 2, p. 425-478.
- Ehlers, T.A. and Farley, K.A., 2003, Apatite (U-Th)/He thermochronometry: methods and applications to problems in tectonic and surface processes: *Earth and Planetary Science Letters*, v. 206, p. 1-14.
- Easterbrook, D.J., 1999, *Surface Processes and Landforms*: Prentice Hall, Upper Saddle River, New Jersey, 546 pp.
- Estabrook, C.H., Nábělek, J.L., and Lerner-Lam, A.L., 1992, Tectonic model of the Pacific-North American plate boundary in the Gulf of Alaska from broadband analysis of the 1979 St. Elias, Alaska, earthquake and its aftershocks: *Journal of Geophysical Research*, v. 97, no. B5, p. 6587-6612.
- Farley, K.A., Wolf, R.A., and Silver, L.T., 1996, The effects of long alpha-stopping distances on (U-Th)/He ages: *Geochimica et Cosmochimica Acta*, v. 60, no. 21, p. 4223-4229.
- Farley, K.A., 2000, Helium diffusion from apatite: General behavior as illustrated by Durango fluorapatite: *Journal of Geophysical Research*, v. 105, no. B2, p. 2903-2914.
- Fletcher, H.J. and Freymueller, J.T., 1999, New GPS constraints on the motion of the Yakutat block: *Geophysical Research Letters*, v. 26, no. 19, p. 3029-3032.

- Hallet, B., Hunter, L., and Bogen, J., 1996, Rates of erosion and sediment evacuation by glaciers: A review of field data and their implications: *Global and Planetary Change*, v. 12, p. 213-235.
- House, M.A., Wernicke, B.P., Farley, K.A. and Dumitru, T.A., 1997, Cenozoic thermal evolution of the central Sierra Nevada from (U-Th)/He thermochronometry: *Earth and Planetary Science Letters*, v. 151, no. 3-4, p. 167-179.
- Jaeger, J.M., Nittrouer, C.A., Scott, N.D., and Milliman, J.D., 1998, Sediment accumulation along a glacially impacted mountainous coastline: north-east Gulf of Alaska: *Basin Research*, v. 10, p. 155-173.
- Jaeger, J.M., Nittrouer, C., and Milliman, J., 2002, Evaluating uplift versus glacial erosion in the Chugach-St. Elias Mountains, south-central Alaska: Answers from Holocene marine strata: *Eos, Transactions, American Geophysical Union*, v. 83, no. 47, Fall Meeting Supplemental, Abstract T12E-09.
- Kirkbride, M. and Matthews, D., 1997, The role of fluvial and glacial erosion in landscape evolution: The Ben Ohau Range, New Zealand: *Earth Surface Processes and Landforms*, v. 22, p. 317-327.
- Koons, P.O., 1995, Modelling the topographic evolution of collisional belts: *Annual Review of Earth and Planetary Sciences*, v. 23, p. 375-408.
- Koppes, M.N. and Hallet, B., 2002, Influence of rapid glacial retreat on the rate of erosion by tidewater glaciers: *Geology*, v. 30, no. 1, p. 47-50.
- Lagoe, M.B., Eyles, C.H., Eyles, N., and Hale, C., 1993, Timing of late Cenozoic tidewater glaciation in the far North Pacific: *Geological Society of American Bulletin*, v. 105, p. 1542-1560.
- Lahr, J.C. and Plafker, G., 1980, Holocene Pacific-North American plate interaction in southern Alaska: Implications for the Yakataga seismic gap: *Geology*, v. 8, no. 10, p. 483-486.
- Lippolt, H.J., Leitz, M., Wernicke, R.S. and Hagedorn, B., 1994, (U+Th)/He dating of apatite: Experience with samples from different geochemical environments: *Chemical Geology*, v. 112, no. 1-2, p. 179-191.
- Long, K.B., 1992, Constraining differential uplift in a brittle, strike-slip fault zone, E. Chugach Mountains, Alaska: University of California at Davis senior thesis.
- Lundgren, P., Saucier, F., Palmer, R., and Langon, M., 1995, Alaska crustal deformation: Finite element modeling constrained by geologic and very long baseline interferometry data: *Journal of Geophysical Research*, v. 100, no. B11, p. 22, 033-22, 045.

- Meigs, A. and Sauber, J., 2000, Southern Alaska as an example of the long-term consequences of mountain building under the influence of glaciers: *Quaternary Science Reviews*, v. 19, p. 1543-1562.
- Molnar, P. and England, P., 1990, Late Cenozoic uplift of mountain ranges and global climate change: chicken or egg?: *Nature*, v. 346, no. 6279, p. 29-34.
- Montgomery, D.R., 1994, Valley incision and the uplift of mountain peaks: *Journal of Geophysical Research*, v. 99, no. B7, p. 13, 913-13, 921.
- O'Sullivan, P.B. and Currie, L.D., 1996, Thermotectonic history of Mt. Logan, Yukon Territory, Canada: implications of multiple episodes of middle to late Cenozoic denudation: *Earth and Planetary Science Letters*, v. 144, p. 251-261.
- O'Sullivan, P.B., Plafker, G., and Murphy, J.M., 1997, Apatite fission-track thermotectonic history of crystalline rocks in the northern Saint Elias Mountains, Alaska, *in* Dumoulin, J.A. and Gray, J.E., eds., *Geological Studies in Alaska by the U.S. Geological Survey, 1995: U.S. Geological Survey Professional Paper 1574*, p. 283-293.
- Page, R.A., 1975, Evaluation of seismicity and earthquake shaking at offshore sites: Houston, Texas, Annual Offshore Technology Conference, 7th, Proceedings, v. 3, p. 179-190.
- Page, R.A., Stephens, C.D., and Lahr, J.C., 1989, Seismicity of the Wrangell and Aleutian Wadati-Benioff zones and the North American plate along the Trans-Alaska Crustal Transect, Chugach Mountains and Copper River basin, southern Alaska: *Journal of Geophysical Research*, v. 94, no. B11, p. 16, 059-16, 082.
- Paterson, W.S.B., 1994, *The Physics of Glaciers*: Elsevier, Tarrytown, 480 pp.
- Péwé, T.L., 1975, Quaternary geology of Alaska: United States Geological Survey, Professional Paper, 145 pp.
- Plafker, G., Hudson, T., and Rubin, M., 1976, Late Holocene offset features along the Fairweather fault: United States Geological Survey Circular, Report: C 0733, p. 57-58.
- Plafker, G., 1987, Regional geology and petroleum potential of the northern Gulf of Alaska continental margin, *in* Scholl, D.W., Grantz, A., and Vedder, J.G., eds., *Geology and resource potential of the continental margin of western North America and adjacent ocean basins-Beaufort Sea to Baja California*: Houston, Texas, Circum-Pacific Council for Energy and Mineral Resources, Earth Science Series, v. 6, p. 229-268.
- Plafker, G., Moore, J.C., and Winkler, G.R., 1994b, Geology of the southern Alaska Margin, *in* Plafker, G. and Berg, H.C., eds., *The Geology of Alaska: The Geology of North America*, Geological Society of America, Boulder, pp. 389-449.

- Porter, S.C., 1989a, Late Holocene fluctuations of the fjord glacier system in Icy Bay, Alaska: *Arctic and Alpine Research*, v. 21, no. 4, p. 364-379.
- Raymo, M.E., Ruddiman, W.F., and Froelich, P.N., 1988, Influence of late Cenozoic mountain building on ocean geochemical cycles: *Geology*, v. 16, no. 7, p. 649-653.
- Reiners, P. and Farley, K.A., 1999, Helium diffusion and thermochronometry of titanite: *Geochimica et Cosmochimica Acta*, v. 63, no. 22, p. 3845-3859.
- Sauber, J., McClusky, S., and King, R., 1997, Relation of ongoing deformation rates to the subduction zone process in southern Alaska: *Geophysical Research Letters*, v. 24, no. 22, p. 2853-2856.
- Savage, J.C. and Lisowski, M., 1988, Deformation in the Yakataga seismic gap, southern Alaska, 1980-1986: *Journal of Geophysical Research*, v. 93, no. B5, p. 4731-4744.
- Sheaf, M.A., Serpa, L., and Pavlis, T.L., 2003, Exhumation rates in the St. Elias Mountains, Alaska: *Tectonophysics*, v. 367, p. 1-11.
- Small, E.E. and Anderson, R.S., 1995, Geomorphically driven late Cenozoic rock uplift in the Sierra Nevada, California: *Science*, v. 270, p. 277-280.
- Tippett, J.M. and Kamp, P.J.J., 1995, Geomorphic evolution of the Southern Alps, New Zealand: *Earth Surface Processes and Landforms*, v. 20, p. 177-192.
- Warnock, A.C., Zeitler, P.K., Wolf, R.A. and Bergman, S.C., 1997, An evaluation of low-temperature apatite U-Th/He thermochronometry: *Geochimica et Cosmochimica Acta*, v. 61, no. 24, p. 5371-5377.
- Whipple, K.X., Kirby, E., and Brocklehurst, S.H., 1999, Geomorphic limits to climate-induced increases in topographic relief: *Nature*, v. 401, p. 39-43.
- Willett, S.D. and Brandon, M.T., 2002, On steady states in mountain belts: *Geology*, v. 30, no. 2, p. 175-178.
- Wolf, R.A., Farley, K.A., and Silver, L.T., 1996, Helium diffusion and low-temperature thermochronometry of apatite: *Geochimica et Cosmochimica Acta*, v. 60, no. 21, p. 4231-4240.
- Wolf, R.A., Farley, K.A., and Kass, D.M., 1998, Modeling of the temperature sensitivity of the apatite (U-Th)/He thermochronometer: *Chemical Geology*, v. 148, p. 105-114.
- Zeitler, P.K., Herczig, A.L., McDougall, I. and Honda, M., 1987, U-Th-He dating of apatite: A Potential thermochronometer: *Geochimica et Cosmochimica Acta*, v. 51, no. 10, p. 2865-2868.

Zeitler, P.K., Koons, P.O., Bishop, M., Chamberlain, C.P., Craw, D., Edwards, M.,
Hamidullah, S., Jan, M.Q., Khan, M.A., Khattak, M.U.K., Kidd, W., Mackie, R., Meltzer, A.,
Park, S., Pecher, A., Poage, M., Sarker, G., Schneider, D., Seeber, L., Shroder, J., 2001,
Crustal reworking at Nanga Parbat, Pakistan: Evidence for erosional focusing of crustal
strain: *Tectonics*, v. 20, p. 712-728.

Vita

Jamie Todd Buscher

Jamie Todd Buscher was born in Fort Huachuca, Arizona, in 1971. He graduated from John Marshall Fundamental High School in Pasadena, California, in 1989. He received an Associate of Applied Science degree from ITT Technical Institute in 1992. He attended Pasadena City College until 1995 and then transferred to the University of California, Los Angeles, where he received a Bachelor of Science degree in Geology in 1998. After working in the geotechnical industry at Hydrologue, Inc. for almost three years, he returned to school at Virginia Tech where he received his Master of Science degree in Geology in 2003. He anticipates publishing his thesis work and pursuing a Ph.D. in Geology.